Applied Mathematical Modelling 151 (2026) 116504

Contents lists available at ScienceDirect

Applied Mathematical Modelling

journal homepage: www.elsevier.com/locate/apm

Isogeometric topology optimization for smooth shells using a conformal mapping-enhanced level set method

Zhi Xing, Yingjun Wang *

National Engineering Research Center of Novel Equipment for Polymer Processing, The Key Laboratory of Polymer Processing Engineering of the Ministry of Education, Guangdong Provincial Key Laboratory of Technique and Equipment for Macromolecular Advanced Manufacturing, South China University of Technology, Guangzhou 510641, China

ARTICLE INFO

Keywords:
Isogeometric analysis
Topology optimization
Kirchhoff-Love shell
Conformal mapping
Level set method

ABSTRACT

Shells demonstrate pronounced geometric dependence, making it essential to maintain precise geometric characterization and well-defined design boundaries during optimization. This study achieves isogeometric topology optimization (ITO) of smooth shells with arbitrary geometric features through the integration of isogeometric analysis (IGA) and level set method (LSM). An analytical model of shells based on Kirchhoff-Love theory is constructed using nonuniform rational B-splines (NURBS) basis functions, ensuring precise geometric representation. Through conformal mapping, 3D smooth shells are transformed into a 2D design domain where LSM-based ITO is executed to optimize configurations with clear boundaries. The IGA framework unifies geometric and analytical models, eliminating conventional geometric approximation errors and enhancing computational accuracy. Numerical experiments confirm that the proposed method significantly improves computational efficiency while preserving geometric integrity of smooth shells, demonstrating exceptional robustness across diverse boundary conditions.

1. Introduction

Shells, characterized by their lightweight and high-performance, are widely used in engineering fields such as aerospace, civil engineering, automotive, and shipbuilding [1–5]. Due to the large length-to-thickness ratio of shells, their analysis differs from that of solid elements. Commonly employed elements include thick shell elements based on the Reissner-Mindlin theory [6], which considers transverse shear deformation, and thin shell elements based on the Kirchhoff-Love theory [7], which assumes that transverse shear deformation is negligible. The Reissner-Mindlin theory only requires only C^0-continuity between shell elements, simplifying the implementation. However, while thin shells are suitable for many engineering applications, they also present implementation challenges. The Kirchhoff-Love theory requires at least C^1-continuity between shell elements, a requirement that conventional polynomial shape functions often cannot satisfy.

Isogeometric analysis (IGA) [8,9] has been widely studied in recent years as a promising approach in computational mechanics, demonstrating its effectiveness in various fields, including structural mechanics, solid mechanics, thermal analysis, and fluid dynamics [10–14]. The inherent smooth continuity of nonuniform rational B-splines (NURBS) [15] has addressed the challenges in constructing Kirchhoff-Love shell elements, thereby facilitating the development of IGA for smooth shells. Kiendl et al. [7] presented the construction theory for Kirchhoff-Love shell elements based on NURBS basis functions, enabling the integration of design and analysis on

* Corresponding author.
E-mail address: wangyj84@scut.edu.cn (Y. Wang).

https://doi.org/10.1016/j.apm.2025.116504
Received 5 June 2025; Received in revised form 24 September 2025; Accepted 13 October 2025
Available online 14 October 2025

the shell. Furthermore, Kiendl and Bazilevs et al. [16] implemented multi-patch IGA for shells by introducing virtual material strips with unidirectional bending stiffness and zero membrane stiffness at patch interfaces. Similarly, Farahata et al. [17] performed isogeometric discretization based on a special class of surface patches, also achieving IGA for multi-patch Kirchhoff-Love shells. Kiendla and Hsub et al. [18] proposed compressible and incompressible hyperelastic formulations based on Kirchhoff-Love shell elements, thus extending the application of IGA for shells to the large strain regime. As research progresses, challenges encountered in finite element analysis (FEM) of shells have received increasing attention within IGA. For instance, Le and Nguyen-Xuan et al. [19] combined the discrete-strain gap (DSG) method with the patch-wise reduced integration to mitigate the membrane locking effect in shells. Leonetti et al. [20] performed large deformation analysis of rotation-free shells with a small number of degrees of freedom by modeling the stiff layers as Kirchhoff-Love shells and the soft core as solid shells. Alaydin and Bazilevs [21] realized the IGA of frictional contact based on the formulation for multi-layer Kirchhoff-Love shells, and improved the nonlinear convergence of the integral process. Mohammadi et al. [22] proposed a simplified IGA suitable for analyzing the free vibration behavior of shells with arbitrary shapes.

In the field of topology optimization (TO) [23–25], IGA is increasingly replacing conventional analysis methods, leading to the development of numerous isogeometric topology optimization (ITO) methods [26–29]. For example, Hassani and Khanzadi et al. [30] first used IGA to complete TO based on the solid isotropic material with penalization (SIMP) method by predefining density at control points. Subsequently, SIMP-based ITO developed rapidly [31–38]. Compared to density-based optimization methods, the level set method (LSM) [39] has attracted considerable attention due to its explicit boundary representation capabilities. Consequently, Shojaee et al. [40] first explored the integration of radial basis function-based LSM with IGA. Furthermore, Wang and Benson [41] unified the basis functions of the parameterized LSM with the NURBS basis functions used in IGA, establishing smooth integration between geometric and analytical models. Subsequently, they discussed arbitrary geometric constraint and cell clipping issues based on the above method [42]. The combination of LSM and IGA provides a high degree of consistency between geometric representation and analysis, resulting in well-defined design boundaries and geometric features. Many scholars have conducted related research based on LSM [43,44]. LSM-based ITO demonstrates inherent advantages when dealing with smooth shells that exhibit high geometric sensitivity. However, as the geometric features of the smooth shell become more complex, the computational cost of LSM will increase. To address this issue, Ye et al. [45] introduced conformal mapping [46–49] into LSM-based TO, revealing for the first time the relationship between shell TO and the 2D Euclidean space. This approach not only reduces computational cost but also simplifies the complexity of algorithmic implementation. Moreover, the effectiveness of conformal mapping-enhanced LSM has been rigorously validated in several engineering fields [50–52].

Therefore, this paper presents a novel ITO for smooth shells with arbitrary geometric features, achieved through the integration of conformal mapping-enhanced LSM with IGA. The Kirchhoff–Love shell element is constructed within the IGA framework using NURBS basis functions. Conformal mapping is then employed to transform the parameter domain of the isogeometric shell onto a 2D Euclidean domain, where the ITO for smooth shells is executed. This method not only benefits from the high accuracy and high-order continuity provided by IGA, but also effectively preserves the geometric features of smooth shells at a low computational cost. Numerical examples demonstrate that the proposed method effectively minimizes the objective function of smooth shells with arbitrary geometric features, while maintaining excellent robustness.

The remainder of this paper is organized as follows: Section 2 details the construction of NURBS basis functions and their application within the IGA for smooth shells. Section 3 elucidates the theoretical foundation of the conformal mapping-enhanced LSM and associated optimization formulations. Then, Section 4 presents the numerical examples. Finally, Section 5 concludes the paper and discusses potential avenues for future research.

2. IGA of the shell based on NURBS

2.1. NURBS basis functions and advantages

IGA [8] is a novel numerical analysis technique that combines NURBS [15] with FEM, utilizing NURBS as the foundation for the analysis model, thus enabling the integration of geometric modeling and physical analysis. The 2D NURBS basis functions can be represented as the tensor product of two NURBS basis functions:

$$R_{i,p}^{j,q}(\xi,\eta) = \frac{N_{i,p}(\xi)N_{j,q}(\eta)\omega_{i,j}}{\sum\limits_{\hat{i}=1}^{n}\sum\limits_{\hat{j}=1}^{m} N_{\hat{i},p}(\xi)N_{\hat{j},q}(\eta)\omega_{\hat{i},\hat{j}}}, \tag{1}$$

where p and q respectively represent the orders of the two basis functions, ξ and η are the corresponding nodes. $\boldsymbol{\Xi}^1 = \left\{\xi_1, \xi_2, \ldots, \xi_{n+p+1}\right\}$ and $\boldsymbol{\Xi}^2 = \{\eta_1, \eta_2, \ldots, \eta_{m+q+1}\}$ are the specific vector representations. $\omega_{i,j}$ is the corresponding weight of the tensor product of basis functions $N_{i,p}(\xi)$ and $N_{j,q}(\eta)$.

By performing a linear combination of 2D NURBS basis functions and control points, the NURBS surface is derived as:

$$\mathbf{S}_N(\xi,\eta) = \sum_{i=1}^{n}\sum_{j=1}^{m} R_{i,p}^{j,q}(\xi,\eta)\mathbf{P}_{i,j}, \tag{2}$$

where $\mathbf{P}_{i,j}$ represents the corresponding control points of the tensor product of the two basis functions, and the orders p and q, and knot vectors $\boldsymbol{\Xi}^1$ and $\boldsymbol{\Xi}^2$ can all be different.

Furthermore, the basis functions of NURBS have advantages in continuity. A p-order NURBS curve is C^{p-k}-continuity within a knot span, where k represents the multiplicity of the knot (i.e., as the knot multiplicity increases, the continuity at the knot decreases). Compared with IGA, conventional FEM predominantly employs Lagrange interpolation function, as shown in Fig. 1, which shows the continuity of NURBS basis function and Lagrange interpolation function.

As shown in Fig. 1(a), the 2-order NURBS basis function maintains complete C^1-continuity across interior intervals. Continuity is reduced to C^{-1} only at the knots with multiplicity k=3 (positions 0 and 3). As shown in Fig. 1(b), the 2-order Lagrange interpolation function exhibits cusp points, which evidently can only maintain C^0-continuity. And, it can also be found in Fig. 1 that based on the advantage of high-order continuity inherent in IGA, equivalent analysis to FEM can be achieved with fewer degrees of freedom. Within a design domain discretized into n×n elements, the IGA method requires only (n+2)×(n+2) control points, while the FEM method necessitates (2n+1)×(2n+1) nodes. Furthermore, the difference in computational cost between the two methods is significant, particularly considering computational units with varying degrees of freedom, which is confirmed in reference [41].

2.2. Isogeometric shells based on Kirchhoff–Love elements

Under the Kirchhoff-Love theory, it is assumed that a straight line initially perpendicular to the mid-surface remains straight and perpendicular to it after deformation. Detailed theory can be found in reference [53]. This section introduces a shell mechanics model based on the Kirchhoff-Love theory for IGA.

As shown in Fig. 2, we define a global coordinate system (x, y, z) and a curvilinear coordinate system (ξ,η,ζ). α represents the mid-surface of the shell, α^{ζ} represents an arbitrary surface in the shell parallel to the mid-surface, and t represents the thickness of the shell. Let the position vector of an arbitrary point on the mid-surface of the shell before and after deformation be represented by $\mathbf{r}$ and $\overline{\mathbf{r}}$, respectively. And the covariant basis vectors on the mid-surface are as follows:

$$\begin{aligned} \mathbf{g}_\alpha &= \mathbf{r}_{,\alpha}, \\ \overline{\mathbf{g}}_\alpha &= \overline{\mathbf{r}}_{,\alpha}, \end{aligned} \tag{3}$$

where the Greek letters take values of 1 and 2, and this convention applies hereafter, corresponding to the parametric directions ξ and η on the mid-surface of shells, respectively. The comma denotes the partial differentiation of the position vector with respect to different parametric directions. And the covariant metric coefficients on the mid-surface are:

$$\begin{aligned} g_{\alpha\beta} &= \mathbf{g}_\alpha \cdot \mathbf{g}_\beta. \\ \overline{g}_{\alpha\beta} &= \overline{\mathbf{g}}_\alpha \cdot \overline{\mathbf{g}}_\beta. \end{aligned} \tag{4}$$

Next, the unit normal vectors on the mid-surface of the shell before and after deformation are defined as follows:

$$\begin{aligned} \mathbf{g}_3 &= \frac{\mathbf{g}_1 \times \mathbf{g}_2}{|\mathbf{g}_1 \times \mathbf{g}_2|}. \\ \overline{\mathbf{g}}_3 &= \frac{\overline{\mathbf{g}}_1 \times \overline{\mathbf{g}}_2}{|\overline{\mathbf{g}}_1 \times \overline{\mathbf{g}}_2|}. \end{aligned} \tag{5}$$

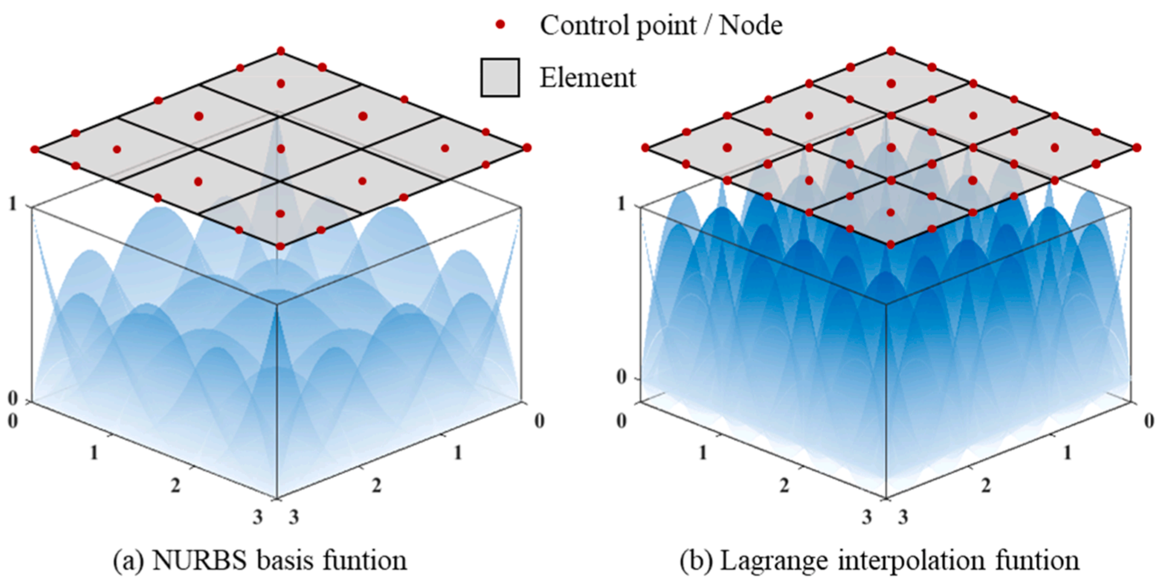

Fig. 1. Construction of IGA and FEM elements.

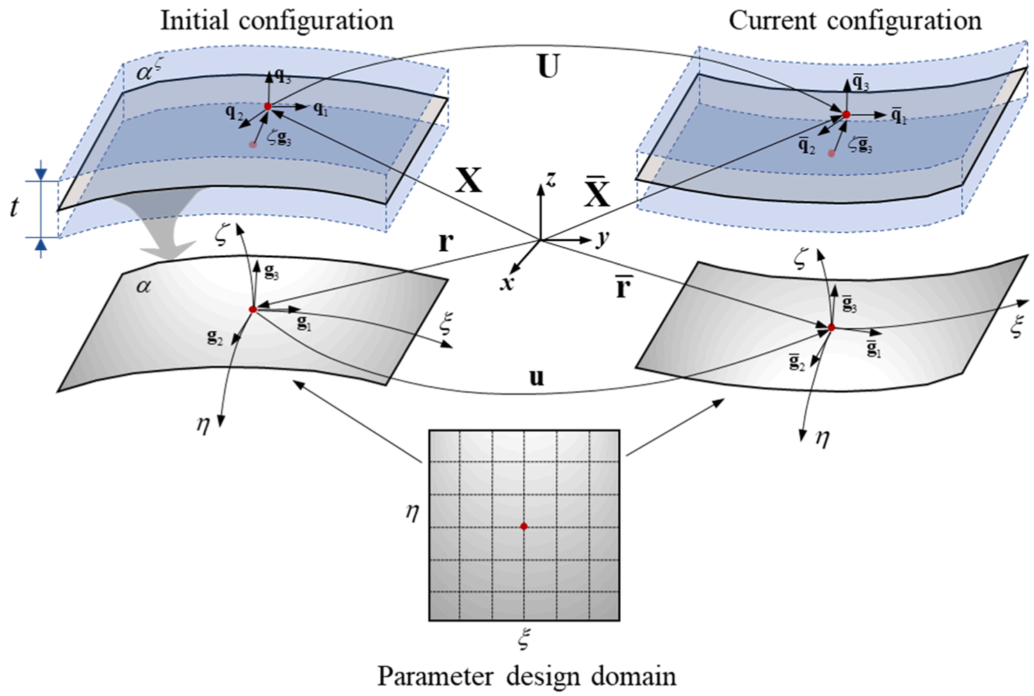

Fig. 2. Description of the Kirchhoff-Love shell.

In Fig. 2, the position vectors of an arbitrary point on the shell before and after deformation are defined as $\mathbf{X}$ and $\overline{\mathbf{X}}$, which can be expressed based on the position vectors $\mathbf{r}$ and $\overline{\mathbf{r}}$ of the mid-surface, as follows:

$$\begin{aligned}\mathbf{X}(\xi,\eta,\zeta) &= \mathbf{r}(\xi,\eta) + \zeta\mathbf{g}_3(\xi,\eta),\\ \overline{\mathbf{X}}(\xi,\eta,\zeta) &= \overline{\mathbf{r}}(\xi,\eta) + \zeta\overline{\mathbf{g}}_3(\xi,\eta),\end{aligned} \tag{6}$$

where ζ represents the distance of the surface from the mid-surface, and it must satisfy condition $-\frac{t}{2} \le \zeta \le \frac{t}{2}$. In Fig. 2, $\zeta\mathbf{g}_3$ and $\zeta\overline{\mathbf{g}}_3$ are visualized, representing the vectors pointing from an arbitrary point on the mid-surface α to its corresponding point on an arbitrary surface α^{ζ}.

Based on Eq. (3), the contravariant base vectors are expressed as:

$$\mathbf{g}^{\alpha}\cdot\mathbf{g}_{\beta} = \overline{\mathbf{g}}^{\alpha}\cdot\overline{\mathbf{g}}_{\beta} = \delta^{\alpha}_{\beta}, \tag{7}$$

where δ^{α}_{β} is Kronecker Delta. Thus, the contravariant metric coefficients can be obtained as:

$$\mathbf{g}^{\alpha} = g^{\alpha\beta}\mathbf{g}_{\beta}.\text{with}[g^{\alpha\beta}] = \left[g_{\alpha\beta}\right]^{-1} \tag{8}$$

According to Eq. (6), the covariant base vectors at any point on the shell are expressed as follows:

$$\begin{aligned}\mathbf{q}_{\alpha} &= \mathbf{X}_{,\alpha} = \mathbf{g}_{\alpha} + \zeta\mathbf{g}_{3,\alpha}.\\ \overline{\mathbf{q}}_{\alpha} &= \overline{\mathbf{X}}_{,\alpha} = \overline{\mathbf{g}}_{\alpha} + \zeta\overline{\mathbf{g}}_{3,\alpha}.\end{aligned} \tag{9}$$

Based on the Kirchhoff-Love theory, $\mathbf{q}_3$ and $\overline{\mathbf{q}}_3$ are defined as follows:

$$\begin{aligned}\mathbf{q}_3 &= \mathbf{X}_{,3} = \mathbf{g}_3.\\ \overline{\mathbf{q}}_3 &= \overline{\mathbf{X}}_{,3} = \overline{\mathbf{g}}_3.\end{aligned} \tag{10}$$

Combining Eqs. (9) and (10), the covariant metric coefficients at any point on the shell are given by:

$$\begin{aligned}q_{ij} &= \mathbf{q}_i\cdot\mathbf{q}_j,\\ \overline{q}_{ij} &= \overline{\mathbf{q}}_i\cdot\overline{\mathbf{q}}_j,\end{aligned} \tag{11}$$

where the Latin indices take values of 1, 2 and 3, and this convention applies hereafter. Furthermore, based on the second fundamental form of the surface, the curvature tensor coefficients of the shell before and after deformation are defined as follows:

$$G_{\alpha\beta} = \frac{1}{2}\left(\mathbf{q}_{\alpha,\beta} \cdot \mathbf{q}_3 + \mathbf{q}_{\beta,\alpha} \cdot \mathbf{q}_3\right) = \mathbf{q}_{\alpha,\beta} \cdot \mathbf{q}_3.$$
$$\overline{G}_{\alpha\beta} = \frac{1}{2}\left(\overline{\mathbf{q}}_{\alpha,\beta} \cdot \overline{\mathbf{q}}_3 + \overline{\mathbf{q}}_{\beta,\alpha} \cdot \overline{\mathbf{q}}_3\right) = \overline{\mathbf{q}}_{\alpha,\beta} \cdot \overline{\mathbf{q}}_3. \tag{12}$$

Reconsidering the position vector in Eq. (6), and using the total Lagrangian formulation, the position vector $\overline{\mathbf{X}}$ of an arbitrary point on the shell after deformation can be expressed in terms of the position vector $\mathbf{X}$ before deformation and the displacement vector $\mathbf{U}$. The same derivation can be made on the mid-surface:

$$\overline{\mathbf{X}}(\xi,\eta,\zeta) = \mathbf{X}(\xi,\eta,\zeta) + \mathbf{U}(\xi,\eta,\zeta).$$
$$\overline{\mathbf{r}}(\xi,\eta) = \mathbf{r}(\xi,\eta) + \mathbf{u}(\xi,\eta). \tag{13}$$

The Green–Lagrange strain tensor can be expressed as:

$$\mathbf{E} = \frac{1}{2}\left(\mathbf{F}^{\mathrm{T}}\mathbf{F} - \mathbf{I}\right) = E_{ij}\mathbf{q}^i \otimes \mathbf{q}^j, \tag{14}$$

where $\mathbf{F}$ represents the deformation gradient, which satisfies condition $\mathrm{d}\overline{\mathbf{X}} = \mathbf{F}\mathrm{d}\mathbf{X}$. In other word, $\mathbf{F}$ represents the Jacobian matrix for the transformation from $\mathbf{X}$ to $\overline{\mathbf{X}}$, and $\mathbf{I}$ is the identity tensor.

Acording to the Kirchhoff-Love theory, $E_{\alpha 3} = 0$ should be satisfied throughout the deformation process. Then, the coefficient E_{ij} in Eq. (14) is expressed as:

$$E_{\alpha\beta} = \frac{1}{2}\left(\overline{q}_{\alpha\beta} - q_{\alpha\beta}\right) = \varepsilon_{\alpha\beta} + \zeta\kappa_{\alpha\beta}, \tag{15}$$

where $\varepsilon_{\alpha\beta}$ and $\kappa_{\alpha\beta}$ represent the membrane strain and bending strain, respectively, with the following specific expressions:

$$\varepsilon_{\alpha\beta} = \frac{1}{2}\left(\overline{\mathbf{g}}_\alpha \cdot \overline{\mathbf{g}}_\beta - \mathbf{g}_\alpha \cdot \mathbf{g}_\beta\right).$$
$$\kappa_{\alpha\beta} = G_{\alpha\beta} - \overline{G}_{\alpha\beta} = \mathbf{g}_{\alpha,\beta} \cdot \mathbf{g}_3 - \overline{\mathbf{g}}_{\alpha,\beta} \cdot \overline{\mathbf{g}}_3. \tag{16}$$

Based on Eq. (13), the relationship between covariant basis vectors of the mid-surface before and after deformation is established as $\overline{\mathbf{g}}_\alpha = \mathbf{g}_\alpha + \mathbf{u}_{,\alpha}$. Substitution into Eq. (16) allows the strain to be expressed in terms of the mid-surface displacements:

$$\varepsilon_{\alpha\beta} = \frac{1}{2}\left(\mathbf{g}_\alpha \cdot \mathbf{u}_{,\beta} + \mathbf{g}_\beta \cdot \mathbf{u}_{,\alpha}\right),$$
$$\kappa_{\alpha\beta} = -\mathbf{u}_{,\alpha\beta} \cdot \mathbf{g}_3 + \frac{1}{\sqrt{g}}\left[\mathbf{u}_{,1} \cdot \left(\mathbf{g}_{\alpha,\beta} \times \mathbf{g}_2\right) + \mathbf{u}_{,2} \cdot \left(\mathbf{g}_1 \times \mathbf{g}_{\alpha,\beta}\right)\right] \tag{17}$$
$$+\frac{\mathbf{g}_3 \cdot \mathbf{g}_{\alpha,\beta}}{\sqrt{g}}\left[\mathbf{u}_{,1} \cdot \left(\mathbf{g}_2 \times \mathbf{g}_3\right) + \mathbf{u}_{,2} \cdot \left(\mathbf{g}_3 \times \mathbf{g}_1\right)\right],$$

where $\sqrt{g} = |\mathbf{g}_1 \times \mathbf{g}_2|$.

2.3. Governing equations for IGA of the shell

The potential energy of the shell is calculated by the following equation:

$$\Pi(\mathbf{u}) = \Pi^{\mathrm{int}}(\mathbf{u}) + \Pi^{\mathrm{ext}}(\mathbf{u}) = \int_\Omega \left(W^m(\boldsymbol{\varepsilon}) + W^b(\boldsymbol{\kappa})\right)\mathrm{d}\Omega - \int_\Omega \mathbf{f} \cdot \mathbf{u}\mathrm{d}\Omega - \int_\Gamma \mathbf{r} \cdot \mathbf{u}\mathrm{d}\Gamma,$$
$$\text{with} W^m(\boldsymbol{\varepsilon}) = \frac{1}{2}\frac{Et}{1-\nu^2}\boldsymbol{\varepsilon} : \mathbf{H} : \boldsymbol{\varepsilon}, \tag{18}$$
$$W^b(\boldsymbol{\kappa}) = \frac{1}{2}\frac{Et^3}{12(1-\nu^2)}\boldsymbol{\kappa} : \mathbf{H} : \boldsymbol{\kappa},$$

where the first integral represents the internal potential energy $\Pi^{\mathrm{int}}(\mathbf{u})$ of the shell, which can be further divided into membrane energy W^m and bending energy W^b. The subsequent two integrals constitute the external potential energy $\Pi^{\mathrm{ext}}(\mathbf{u})$ of the shell, arising from the surface load vector $\mathbf{f}$ and the edge load vector $\mathbf{r}$.

In the expression for the internal potential energy, E is Young's modulus, ν is the Poisson's ratio, and $\mathbf{H}$ is the elasticity tensor. Based on the contracted notation, the specific expression for $\mathbf{H}$ is as follows:

$$\mathbf{H} = H^{\alpha\beta\gamma\delta}\mathbf{g}_\alpha \otimes \mathbf{g}_\beta \otimes \mathbf{g}_\gamma \otimes \mathbf{g}_\delta.$$
$$H^{\alpha\beta\gamma\delta} = \nu g^{\alpha\beta}g^{\gamma\delta} + \frac{1}{2}(1-\nu)\left(g^{\alpha\gamma}g^{\beta\delta} + g^{\alpha\delta}g^{\beta\gamma}\right). \tag{19}$$

In Eq. (18), using $\mathbf{n}$ to represent the membrane stress tensor and $\mathbf{m}$ to represent the bending stress tensor, the specific expression becomes:

$$\begin{aligned}\mathbf{n}&=\frac{Et}{1-\nu^2}\mathbf{H}:\boldsymbol{\varepsilon}.\\ \mathbf{m}&=\frac{Et^3}{12(1-\nu^2)}\mathbf{H}:\boldsymbol{\kappa}.\end{aligned}\tag{20}$$

According to the principle of virtual work, the displacement vector $\mathbf{u}$ must satisfy the equilibrium condition of minimum potential energy, thereby deriving the variational form of Eq. (18):

$$\delta\Pi=\frac{\partial\Pi}{\partial\mathbf{u}}\delta\mathbf{u}=\int_\Omega\delta\boldsymbol{\varepsilon}:\mathbf{n}+\delta\boldsymbol{\kappa}:\mathbf{m}\mathrm{d}\Omega+\delta\Pi^{\mathrm{ext}}(\mathbf{u})=0.\tag{21}$$

Furthermore, the matrix form of the equilibrium equations is derived as:

$$\begin{aligned}&\mathbf{K}\mathbf{u}=\mathbf{f},\\ &\text{with}\mathbf{K}=\sum_{e=1}^{N}\mathbf{K}_e=\sum_{e=1}^{N}\int_{\Omega^e}\left[(\mathbf{B}^m)^{\mathrm{T}}\mathbf{D}^m\mathbf{B}^m+\left(\mathbf{B}^b\right)^{\mathrm{T}}\mathbf{D}^b\mathbf{B}^b\right]t\mathrm{d}\Omega,\\ &\mathbf{f}=\sum_{e=1}^{N}\left[\int_{\Omega^e}\mathbf{N}^{\mathrm{T}}\mathbf{f}t\mathrm{d}\Omega+\int_{\Omega^e}\mathbf{N}^{\mathrm{T}}\mathbf{r}t\mathrm{d}\Omega\right],\end{aligned}\tag{22}$$

where N represents the number of elements, $\mathbf{K}_e$ denotes the element stiffness matrix, and Ω^e signifies the design domain of the element. $\mathbf{B}^m$ and $\mathbf{B}^b$ represent the strain matrices for the membrane and bending elements, respectively, and are composed of differential operators and interpolation functions $\mathbf{N}$. $\mathbf{D}^m$ and $\mathbf{D}^b$ denote the elasticity matrices for the membrane and bending elements, respectively, and are derived from Eq. (18).

Based on IGA, the displacement vector $\mathbf{u}$ of the shell can be represented by NURBS basis functions and the displacement $\mathbf{u}_{i,j}$ of the control points, as shown in the following expression with reference to Eq. (2):

$$\mathbf{u}(\xi,\eta)=\sum_{i=1}^{n}\sum_{j=1}^{m}R_{i,p}^{j,q}(\xi,\eta)\mathbf{u}_{i,j}.\tag{23}$$

Substituting the above expression into Eq. (22) completes the derivation of the IGA for the shell. This means the interpolation function $\mathbf{N}$ is constructed using $R_{i,p}^{j,q}(\xi,\eta)$.

3. TO based on conformal mapping-enhanced LSM

3.1. Conformal mapping-enhanced LSM

According to the definition of conventional LSM, as shown in Fig. 3, the boundary of the shell within the design domain is represented by the zero-level surface or contour surface of a level set function in a higher dimension. The specific formula is expressed as follows:

$$\begin{cases}\Phi(x,t)>0,\forall x\in\Omega\setminus\partial\Omega,\\ \Phi(x,t)=0,\forall x\in\partial\Omega,\\ \Phi(x,t)<0,\forall x\in D\setminus\Omega,\end{cases}\tag{24}$$

where $\Phi(x,t)$ represents the level set function, x represents the spatial coordinates within the design domain, and t represents time; D is a fixed pre-defined domain, Ω is the solid domain, and $\partial\Omega$ is the dynamic boundary evolving with time.

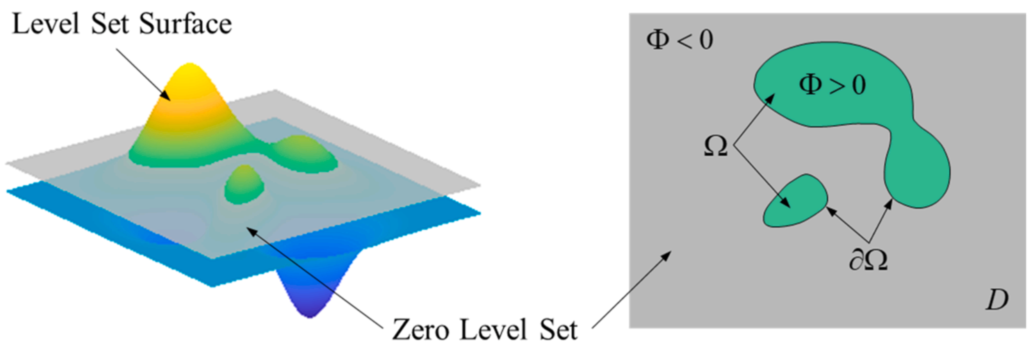

Fig. 3. The description of level set function.

Differentiating Eq. (24) with respect to time yields the Hamilton-Jacobi equation [54]:

$$\frac{\partial \Phi}{\partial t} - \mathbf{V}^{\mathrm{n}} \cdot |\nabla \Phi| = 0, \tag{25}$$

where $\mathbf{V}^{\mathrm{n}}$ represents the normal velocity on the boundary of the level set function.

Conformal geometry theory [48] provides a conformal transformation method between Riemannian and Euclidean spaces, namely conformal mapping, and the algorithm implementation can be found in references [55–57]. Therefore, the level set function in 2D Euclidean space can be extended to Riemannian space. According to Eq. (25), $\nabla\Phi$ is defined in 2D Euclidean space, which can be regarded as a curved surface $\mathbf{R}$. Based on conformal geometry theory, a mapping f :R→M with a conformal factor $e^{2\omega}$ reveals the relationship between $\nabla\Phi$ and Riemannian space M [49]. Therefore, Eq. (25) can be rewritten as:

$$\frac{\partial \Phi}{\partial t} - \mathbf{V}_M^{\mathrm{n}} \cdot |\nabla_M \Phi| = 0, \tag{26}$$

where $\mathbf{V}_M^{\mathrm{n}}$ is the normal velocity field on the Riemannian surface, and $\nabla_M\Phi$ is the gradient of the level set function Φ in Riemannian space. References [45,51] establish the relationship between Riemannian gradients and Euclidean differential operators:

$$\nabla_M f = e^{-2\omega}\frac{\partial f \circ \varphi}{\partial x} + e^{-2\omega}\frac{\partial f \circ \varphi}{\partial y}. \tag{27}$$

where $\circ$ is the composite operation of mappings.

Then, we can rewrite the Hamilton-Jacobi equation:

$$\frac{\partial \Phi}{\partial t} - e^{2\omega}\mathbf{V}^{\mathrm{n}} \cdot |\nabla \Phi| = 0. \tag{28}$$

Using the conformal factor, correct the normal velocity field to the 2D Euclidean space, and solve it on the 2D domain.

In the conventional LSM, the normal velocity field is obtained through the steepest descent method, typically implemented via Lagrange equations for constraint enforcement. Consequently, the update strategy of the Lagrange multipliers directly affects the optimization stability and convergence effect, especially when multiple constraints are involved.

In this work, we employ the velocity field LSM [58,59]. The normal velocity field $\mathbf{V}^{\mathrm{n}}$ of the level set function in Eq. (25) can be constructed by a set of velocity design variables and given basis functions:

$$\mathbf{V}^{\mathrm{n}}(\mathbf{x}) = \sum_{i=1}^{m\times n} \beta_i N_i(\mathbf{x}), \tag{29}$$

where $\beta_i (i = 1, 2, ..., m \times n)$ is the velocity design variables at $m \times n$ control points distributed throughout the design domain, and $N_i(\mathbf{x})$ is the NURBS basis functions, according to Eq. (23).

In this way, the solution of normal velocity field $\mathbf{V}^{\mathrm{n}}$ required for boundary evolution can be transformed into the determination of nodal velocities during each iteration. Simultaneously, sensitivity calculations must be performed within the support domains of corresponding basis functions, while the evaluation of basis function values at Gaussian integration points is also required. Relevant derivations will be presented in the subsequent chapter.

3.2. Optimization model and sensitivity analysis

Without loss of generality, we present the optimization model based on the minimum compliance problem:

$$\begin{aligned}
&\text{Find} : \boldsymbol{\beta} = \{\beta_1, \beta_2, ..., \beta_m\}^{\mathrm{T}},\\
&\min : J = \int_\Omega \mathbf{u}^{\mathrm{T}}\mathbf{K}\mathbf{u}H(\Phi)\mathrm{d}\Omega,\\
&\text{s.t.} : G = \int_\Omega H(\Phi)\mathrm{d}\Omega - V^* \le 0,\\
&a(\mathbf{u}, \overline{\mathbf{u}}, \Phi) = l(\overline{\mathbf{u}}, \Phi), \forall \overline{\mathbf{u}} \in U_{ad},\\
&\mathbf{u} = 0, \mathrm{in}\Gamma_{\mathrm{D}}\\
&\underline{\beta} \le \beta_i \le \overline{\beta}, i = 1, 2, ..., m
\end{aligned} \tag{30}$$

where $\overline{\mathbf{u}}$ is the test function for displacement, $V(\Omega)$ is the volume of the optimized object, and V^* is the target volume. And $H(\Phi)$ is the Heaviside function, U_{ad} is the space kinematically admissible displacement. $\mathbf{u} = 0$ is the constraint that needs to be satisfied at the Dirichlet boundary Γ_{D}. Upper and lower bound constraints are imposed on the velocity design variable β to ensure its physical feasibility and to guarantee the satisfaction of the CFL condition.

In the constraint conditions, a and l are represented as follows:

$$a(\mathbf{u},\overline{\mathbf{u}},\Phi) = \int_\Omega \mathbf{u}^{\mathrm{T}}\mathbf{K}\overline{\mathbf{u}}H(\Phi)\mathrm{d}\Omega,$$
$$l(\overline{\mathbf{u}},\Phi) = \int_\Omega \mathbf{p}\cdot\overline{\mathbf{u}}H(\Phi)\mathrm{d}\Omega + \int_{\Gamma_{\mathrm{N}}} \mathbf{t}\cdot\overline{\mathbf{u}}\mathrm{d}\Gamma, \tag{31}$$

where $\mathbf{p}$ denotes the body force in the material domain Ω, $\mathbf{t}$ denotes the surface traction on the Neumann boundary Γ_{N}.

By employing the augmented Lagrangian method, the given optimization problem can be transformed into an unconstrained optimization problem:

$$L(\mathbf{u},\overline{\mathbf{u}},\Phi) = J(\mathbf{u},\Phi) + a(\mathbf{u},\overline{\mathbf{u}},\Phi) - l(\overline{\mathbf{u}},\Phi) + \lambda G, \tag{32}$$

where λ is the Lagrange multiplier, which iterates with the solution of the formula.

Then, the material derivative of Eq. (32) with respect to a pseudo time t is formulated as follows:

$$\frac{dL(\mathbf{u},\overline{\mathbf{u}},\Phi)}{dt} = \frac{\partial L(\mathbf{u},\overline{\mathbf{u}},\Phi)}{\partial t} + \frac{\partial J(\mathbf{u},\overline{\mathbf{u}},\Phi)}{\partial\Omega}. \tag{33}$$

The partial derivative of time is the adjoint equation, which is expressed as:

$$\frac{\partial L(\mathbf{u},\overline{\mathbf{u}},\Phi)}{\partial t} = 2\int_\Omega (\mathbf{u}^{\mathrm{T}})'\mathbf{K}\mathbf{u}H(\Phi)\mathrm{d}\Omega + \int_\Omega (\mathbf{u}^{\mathrm{T}})'\mathbf{K}\overline{\mathbf{u}}H(\Phi)\mathrm{d}\Omega, \tag{34}$$

by solving the adjoint equation, the adjoint variable $\overline{\mathbf{u}} = -2\mathbf{u}$ can be obtained.

The partial derivative of the domain, which constitute the shape derivative, is expressed as:

$$\frac{\partial J(\mathbf{u},\overline{\mathbf{u}},\Phi)}{\partial\Omega} = \int_\Gamma \mathbf{u}^{\mathrm{T}}\mathbf{K}\mathbf{u}H(\Phi)\mathbf{V}^{\mathrm{n}}\mathrm{d}\Gamma + \int_\Gamma \mathbf{u}^{\mathrm{T}}\mathbf{K}\overline{\mathbf{u}}H(\Phi)\mathbf{V}^{\mathrm{n}}\mathrm{d}\Gamma - \int_\Gamma \mathbf{p}\cdot\overline{\mathbf{u}}H(\Phi)\mathbf{V}^{\mathrm{n}}\mathrm{d}\Gamma - \int_\Gamma \left[\frac{\partial(\mathbf{t}\cdot\overline{\mathbf{u}})}{\partial n} + \kappa(\mathbf{t}\cdot\overline{\mathbf{u}})\right]\mathbf{V}^{\mathrm{n}}\mathrm{d}\Gamma + \lambda\int_\Gamma \mathbf{V}^{\mathrm{n}}\mathrm{d}\Gamma, \tag{35}$$

where $\kappa = \mathrm{div}n$ is the curvature of the boundary. In particular, the Neumann boundary Γ_{N} and the Dirichlet boundary Γ_{D} are often fixed during the optimization process, so the corresponding terms will disappear. We substitute the adjoint variable into Eq. (35), so that Eq. (33) is abbreviated as:

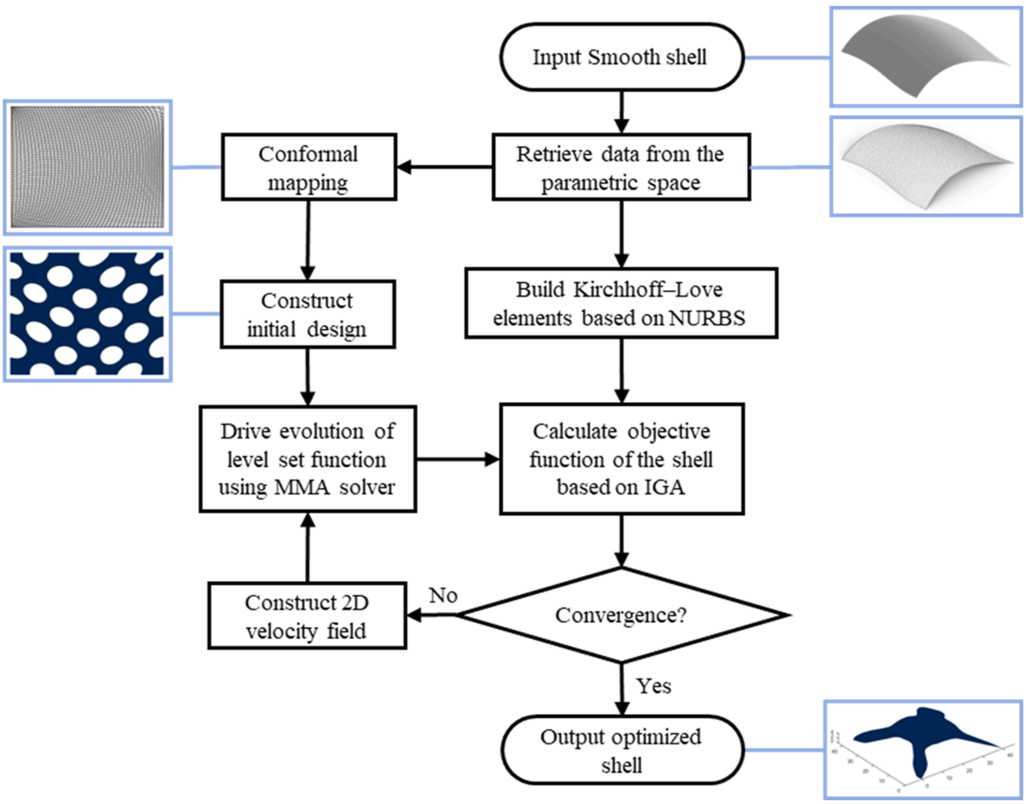

Fig. 4. The flowchart of ITO for smooth shells using a conformal mapping-enhanced LSM.

$$\begin{aligned}&\frac{dL(\mathbf{u},\overline{\mathbf{u}},\Phi)}{dt}=\int_{\Gamma}f(\mathbf{u},\Phi)\mathbf{V}^{\mathrm{n}}\mathrm{d}\Gamma\\&\text{with}f(\mathbf{u},\Phi)=-\mathbf{u}^{\mathrm{T}}\mathbf{K}\mathbf{u}H(\Phi)+2\mathbf{p}\cdot\mathbf{u}H(\Phi)+\lambda.\end{aligned}\tag{36}$$

Based on the transformation relationship between boundary integral and domain integral, Eq. (36) is rewritten as:

$$\frac{dL(\mathbf{u},\overline{\mathbf{u}},\Phi)}{dt}=\int_{\Omega}f(\mathbf{u},\Phi)\delta(\Phi)|\nabla\Phi|\mathbf{V}^{\mathrm{n}}\mathrm{d}\Omega,\tag{37}$$

where $\delta(\Phi)$ is the derivative of Heaviside function. Review Eq. (29), and substitute it into the above equation to get:

$$\frac{dL(\mathbf{u},\overline{\mathbf{u}},\Phi)}{dt}=\sum_{i=1}^{m\times n}\int_{\Omega}f(\mathbf{u},\Phi)\delta(\Phi)|\nabla\Phi|N_i(\mathbf{x})\beta_i\mathrm{d}\Omega.\tag{38}$$

On the other hand, we can use the chain rule to re-derive the Lagrange Eq. (32):

$$\frac{dL(\mathbf{u},\overline{\mathbf{u}},\Phi)}{dt}=\sum_{i=1}^{m\times n}\frac{\partial J}{\partial\beta_i}+\lambda\sum_{i=1}^{m\times n}\frac{\partial G}{\partial\beta_i}.\tag{39}$$

By comparing the correspondence between Eqs. (38) and (39), the sensitivity of the objective function and the constraint can be given respectively:

$$\begin{aligned}&\frac{\partial J}{\partial\beta_i}=\int_{\Omega}\left[2\mathbf{p}\cdot\mathbf{u}-\mathbf{u}^{\mathrm{T}}\mathbf{K}\mathbf{u}\right]\delta(\Phi)|\nabla\Phi|N_i(\mathbf{x})\mathrm{d}\Omega.\\&\frac{\partial G}{\partial\beta_i}=\int_{\Omega}\delta(\Phi)|\nabla\Phi|N_i(\mathbf{x})\mathrm{d}\Omega.\end{aligned}\tag{40}$$

3.3. Implementation

The algorithmic implementation of ITO for smooth shells based on the conformal mapping-enhanced LSM is shown in Fig. 4. Starting from the input smooth shell, data is extracted from the isogeometric parametric domain for conformal mapping, and an initial design is constructed in the 2D domain. Simultaneously, IGA of the shell is performed based on the Kirchhoff–Love theory, and the velocity field required for evolution is constructed based on the analysis results. Then, the IGA and level set evolution are repeated to complete the optimization loop. The loop ends when the following conditions are met: (1) maximum objective function error across last four iterations $< 10^{-5}$ and volume fraction deviation from target $< 10^{-3}$; (2) maximum iteration count reached. Finally, the optimized result is inversely mapped to the 3D domain to output the optimized shell.

Furthermore, conformal mapping needs to be explained in detail. As described in Section 3.1, numerous codes of conformal mapping have been publicly released, including those based on MATLAB [56,57], C++ [55], and so on. To ensure the ease of use and

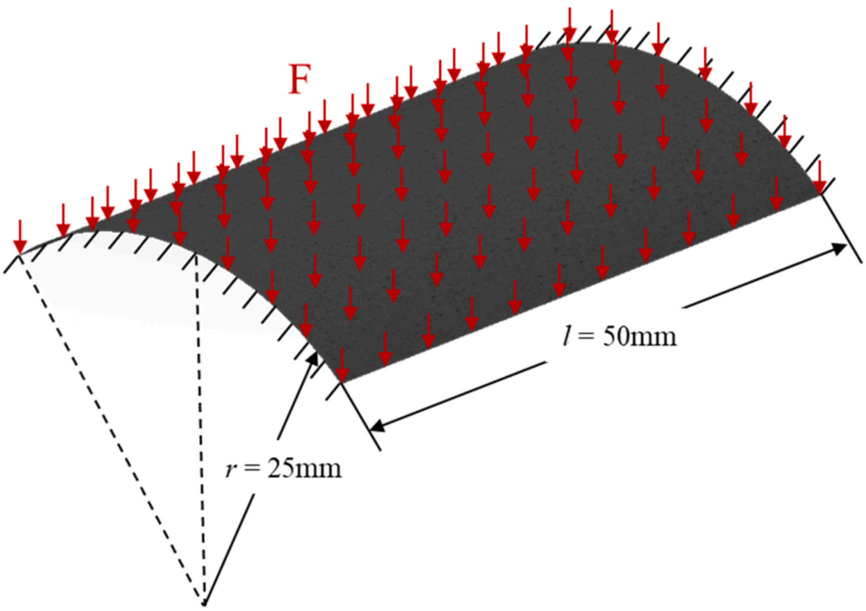

Fig. 5. Design domain of the Scordelis–Lo Roof.

reproducibility of the code, the MATLAB-based code used in this paper, along with its source, can be found on the personal website of the author of reference [56].

4. Numerical examples

To demonstrate the robustness of the proposed method, we present optimized results for smooth shell with varying geometric features, based on the minimum compliance problem. Furthermore, to ensure the data reliability of the numerical examples, we provide necessary parameter specifications. Work environment: CPU is a AMD Ryzen 5 5600 G with Radeon Graphics 3.90 GHz, the RAM is 16 GB and the software is MATLAB R2024a. Except for the specific material parameters of the Scordelis–Lo Roof used for IGA validation, the material parameters for the remaining smooth shells are: Young's modulus $E = 1 \times 10^6$Pa, Poisson's ratio $\nu = 0.3$. And a 6×6 Gauss quadrature integration scheme was employed for all numerical examples. The method of moving asymptotes (MMA) [60] is employed as the optimizer.

All geometric files for the examples are included in Supplementary Materials.

4.1. IGA of Scordelis–Lo Roof

The Scordelis–Lo Roof is a widely popular benchmark example in the field of analysis. To validate the accuracy of the IGA used in this method, we analyzed the Scordelis–Lo Roof based on the parameter configuration of this benchmark example. The detailed size and boundary conditions of the design domain, including the boundary conditions $u_x = u_z = 0$ on both sides of the roof and the uniformly distributed load $F = 90$N, are illustrated in Fig. 5. Material parameters and isogeometric modeling parameters are presented in Table 1.

The most frequently displayed test result is the vertical displacement at the midpoint of the free edge. The theoretical value for this result, as given in the reference [61], is 0.3086; however, most elements converge to a slightly lower value. We show the vertical displacement results for IGA in Fig. 6, with the maximum displacement result being 0.3077, which is close to the theoretical value.

4.2. Validation using classic examples

The paraboloid shell is a classic example in the field of shell optimization, and it serves to demonstrate the effectiveness of the method proposed in this paper. According to references [62–64], we set parameters similar to them to ensure the reliability of the optimized results. The design domain for the paraboloid shell is depicted in Fig. 7(a), with a thickness of 1. Fixed constraints are applied to the four corner points, and a concentrated downward vertical load $F = 100$N is applied at the center. The paraboloid shell is discretized into 59×59 2-order NURBS elements, and the target volume is set to 0.3. Fig. 7(b) shows the initial design used for the paraboloid shell, employing a staggered arrangement of holes which demonstrated good evolutionary performance. In order to avoid matrix singularity and compliance anomalies, the design avoided the highlighted constraint regions in the figure.

Fig. 8(a) illustrates the optimized results, which were subsequently subjected to simulation analysis using Abaqus. Compared with the analysis results of the initial design, as shown in Fig. 8(b), the optimized shell exhibited a significant reduction in displacement, thus demonstrating the effectiveness of the proposed method.

For comparative validation, we also present the optimized results of paraboloid shell from previous studies, as shown in Fig. 9. Fig. 9(a) illustrates the optimized result obtained by Zhang et al. [63] using their proposed T-splines-oriented isogeometric topology optimization method. It can be observed that the structure obtained in this study is very similar to Zhang, forming a typical four-bar truss-like structure that demonstrates the most direct load transfer path from the central load to the four fixed supports. Fig. 9(b) and (c) illustrate optimized results that combine both shape and topology, derived from the studies by Cai et al. [64] and Thuan et al. [62], respectively. The difference from this study is that they consider shape optimization, so the truss features are more obvious, and the middle loading area has obvious prominent features to facilitate the transmission of load.

4.3. Verify the effectiveness of the initial design

LSM-based ITO exhibits some dependence on the initial design, with different initial designs affecting the convergence speed and final results. In this section, we consider the influence of the initial design on the minimum compliance optimization based on a hyperboloid shell.

As shown in Fig. 10, the thickness of the hyperboloid shell is 1. Fixed constraints are applied to the four corner points, and a

Table 1
Related parameters of the Scordelis–Lo Roof.

Young's modulus	Poisson's ratio	Degrees of NURBS	Number of control points	Number of IGA elements	Open knot vectors
$E = 432$ MPa	$\nu = 0$	$p = 3$ $q = 3$	61 × 41	58 × 38	$\Xi^1 = [0, 0, 0, 0, 0.01724, 0.03448, ..., 0.96552, 0.98276, 1, 1, 1, 1]$ $\Xi^2 = [0, 0, 0, 0, 0.02632, 0.05263, ..., 0.94737, 0.97368, 1, 1, 1, 1]$

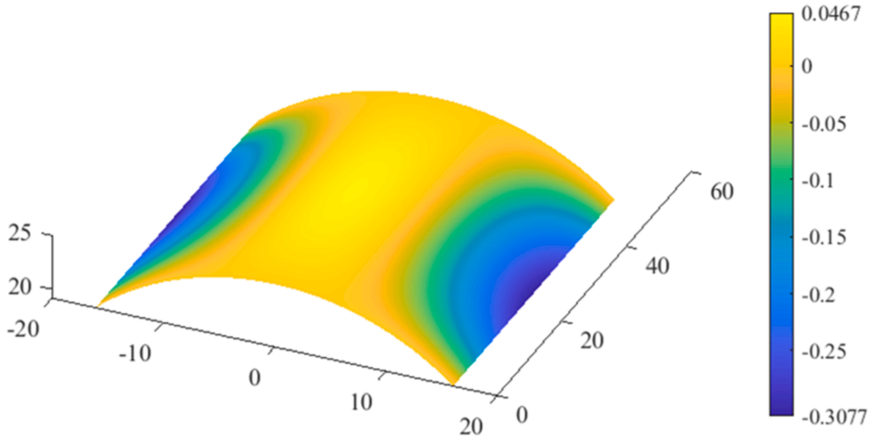

Fig. 6. Vertical displacement field of the Scordelis–Lo Roof.

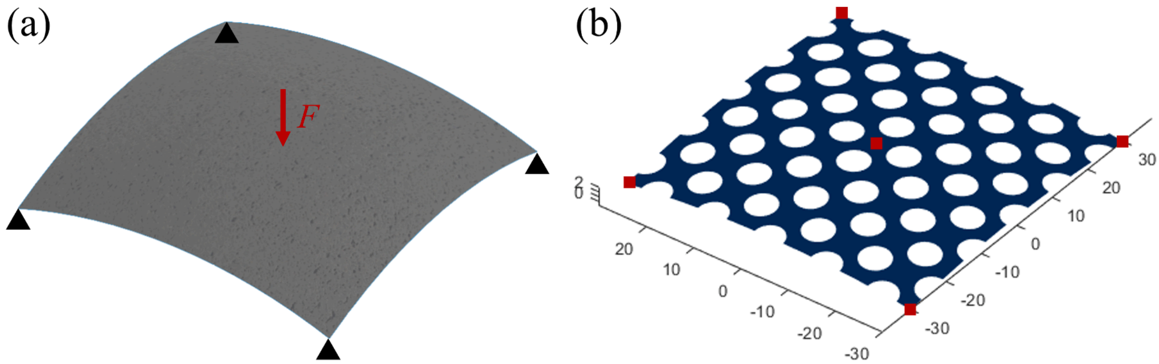

Fig. 7. Design domain of paraboloid shell.

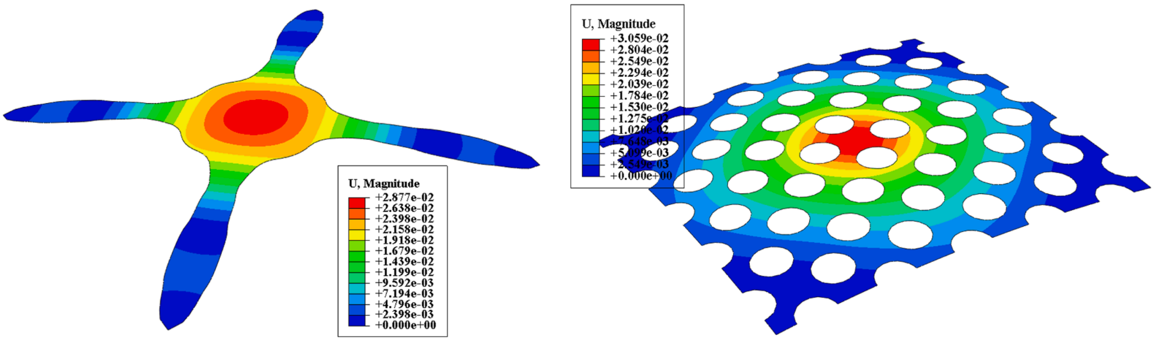

(a) Optimized paraboloid shell (b) Initial design

Fig. 8. Optimized result and simulation analysis of paraboloid shell.

concentrated downward vertical load $F = 1000\text{N}$ is applied at the center. The hyperboloid shell is divided into 33×33 2-order NURBS elements, with the optimized target volume being 0.75. Based on the NURBS parameters of the hyperboloid shell, it is conformally mapped to a 2D domain, and a connectivity mesh of control points is established, as shown by the gray mesh in the figure. The initial design required for LSM-based ITO is then created based on the control point mesh in the 2D domain, as shown by the blue shape in the figure.

We selected several different initial designs, as shown in Fig. 11, and provided the optimized results, number of iterations, and final compliance for each. With an increasing number of holes, the number of iterations decreased to some extent, i.e.,

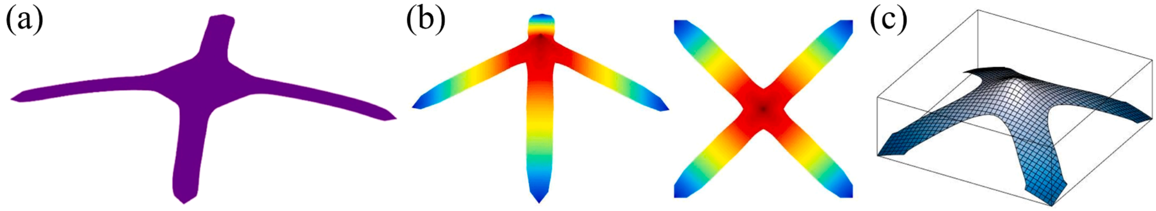

Fig. 9. Optimized results of paraboloid shell in previous studies.

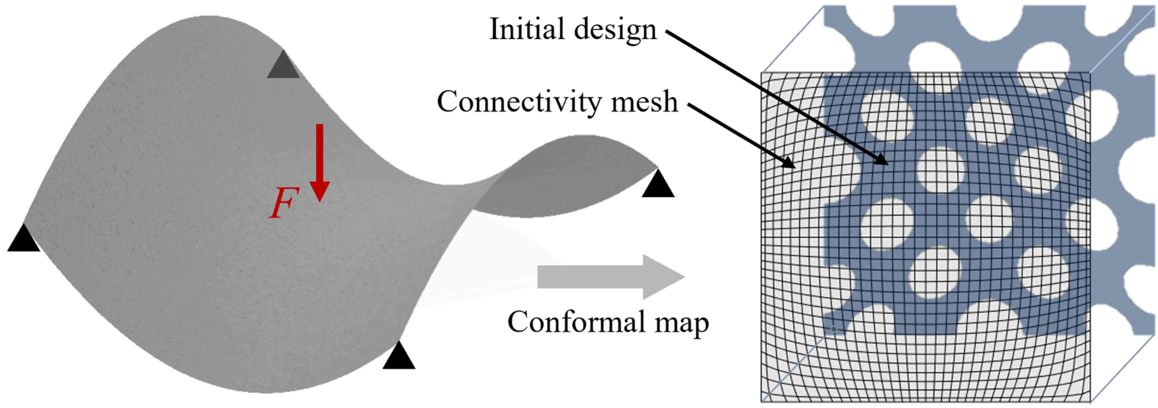

Fig. 10. Design domain of hyperboloid shell.

TypeA ≥ TypeB ≥ TypeC ≥ TypeD, verifying that the LSM is based on the evolution of free boundaries, and that the number of free boundaries influences optimization efficiency to a certain degree. Comparing Type C and Type D, the staggered arrangement of holes is superior to the orthogonal arrangement, which is more conducive to the merging of free boundaries to achieve topological structure changes. Of course, too many free boundaries can add a burden to the evolution, as seen in Type E.

In the proposed LSM-based ITO, different initial designs have a noticeable impact on the number of iterations, but the effect on the final optimized result is not significant. As shown in Fig. 11, the optimized results for different initial designs are similar, and the corresponding compliance values are also close.

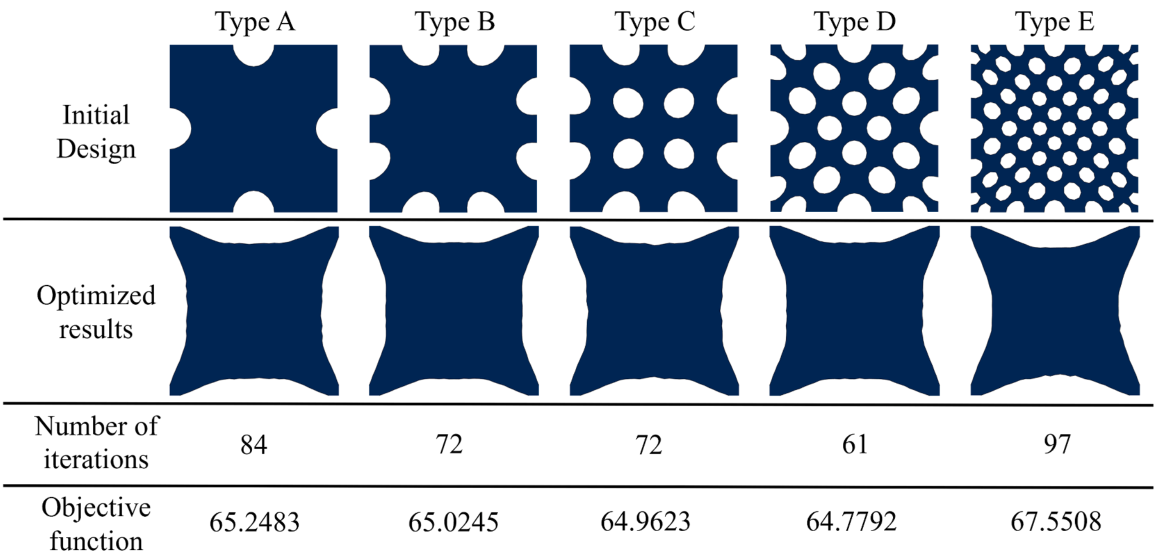

Fig. 11. Optimized results of different initial designs.

4.4. Mesh-dependence

In the field of TO, mesh-dependence has always been a significant topic of discussion. The mesh-dependence problem refers to obtaining qualitatively different solutions for different mesh-sizes or diseretizations. In this paper, we verify the mesh-dependence of the method based on the classical paraboloid shell. The design domain for the paraboloid shell is depicted in Fig. 7(a), with a thickness of 1. Fixed constraints are applied to the four corner points, and a concentrated downward vertical load $F = 100$N is applied at the center, and the target volume is set to 0.5. The initial design also maintained the configuration shown in Fig. 7(b).

As shown in Fig. 12, the number of 2-order NURBS elements increased from 59×59 to 239×239, with the historical and final optimized results displayed sequentially. According to the final results, it is confirmed that this method exhibits mesh-dependence. A noticeable topological change occurred when the size of mesh increased from 89×89 to 119×119, leading to the formation of a more refined structure. It is worth noting that a trend towards generating fine structures is already observed in the historical results of the 89×89 mesh, and simultaneously, with the increase of the number of elements, the configuration of the final results tends to stabilize.

As is well known, traditional optimization problems are often difficult to solve directly for exact solutions, and thus we typically employ discrete methods to establish a solvable new problem. Clearly, mesh-dependence is an inevitable consequence of discretizing optimization problems. Increasing the size of mesh merely helps to approximate the exact solution, and consequently, as the solution changes, the structure inevitably changes. Sigmund and Petersson [65] point out that refinement of the mesh invariably leads to increasingly finer structures, eventually tending towards microstructures. The structural changes observed in this study are consistent with the conclusions of previous research.

4.5. Validity verification based on different design domains

To verify the effectiveness of the proposed LSM-based ITO in maintaining the geometric features of smooth shells, we modeled smooth shells with different geometric features and then performed LSM-based ITO based on the minimum compliance problem.

4.5.1. Curved shell

As shown in Fig. 13(a), a curved shell model is created by sweeping a circular arc along a curved line, and the thickness is 1. Fixed constraints are applied to the four corner points, and a concentrated downward vertical load $F = 1000$N is applied to the center. The model is divided into 119×119 2-order NURBS elements, and the target volume for optimization is 0.5. Fig. 13(b) shows the initial design used for the curved shell, employing a staggered arrangement of holes which demonstrated good evolutionary performance. In order to avoid matrix singularity and compliance anomalies, the design avoided the highlighted constraint regions in the figure.

The historical and final optimized results of the curved shell are presented in Fig. 14. In the initial five iterations, material is rapidly removed to satisfy the volume constraint. After 20 iterations, the structure stabilized, and no superfluous boundaries are generated, which means that only minor adjustments are made to the model's boundaries, with the process ultimately concluding at the 144th iteration. The final optimized result is then inverse-mapped to obtain the optimized curved shell in 3D space.

The optimization curve of the curved shell is illustrated in Fig. 15. In the initial phase of optimization, as the volume rapidly decreases, the strain energy shows a slight increase. As material migrates towards the central region, the strain energy gradually decreases. When the strain energy drops to its minimum, the volume gradually approaches the target volume. After 20 iterations, both the objective function and volume ratio tend to stahbilize, indicating that the curved shell no longer undergoes significant topological changes. Subsequent iterations then continuously fine-tune the structure to reach the optimal result.

4.5.2. Scordelis–Lo Roof. As shown in Fig. 16(a), the Scordelis–Lo Roof is formed by extruding an arc, with a thickness of 1. We

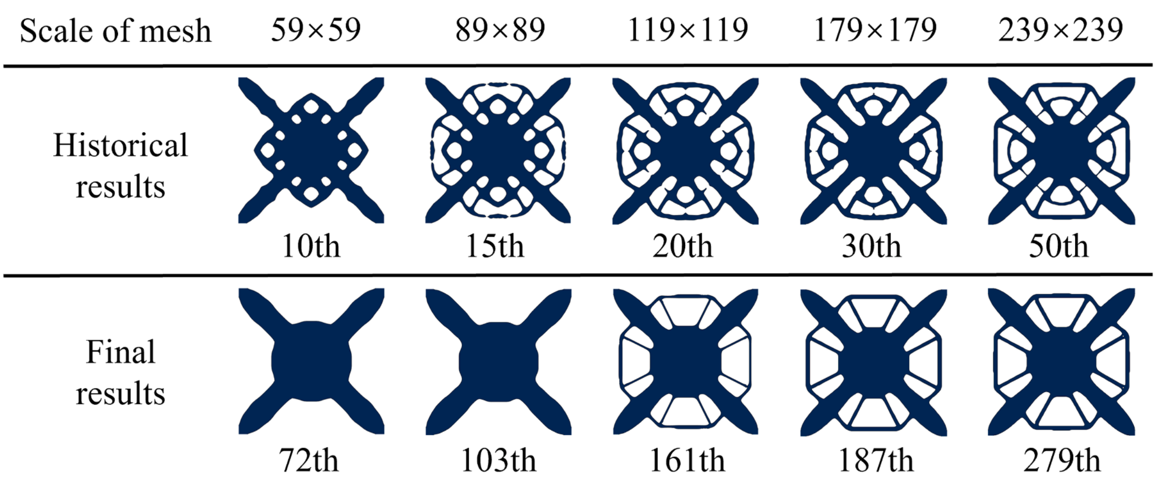

Fig. 12. Historical and final results based on meshes of different sizes.

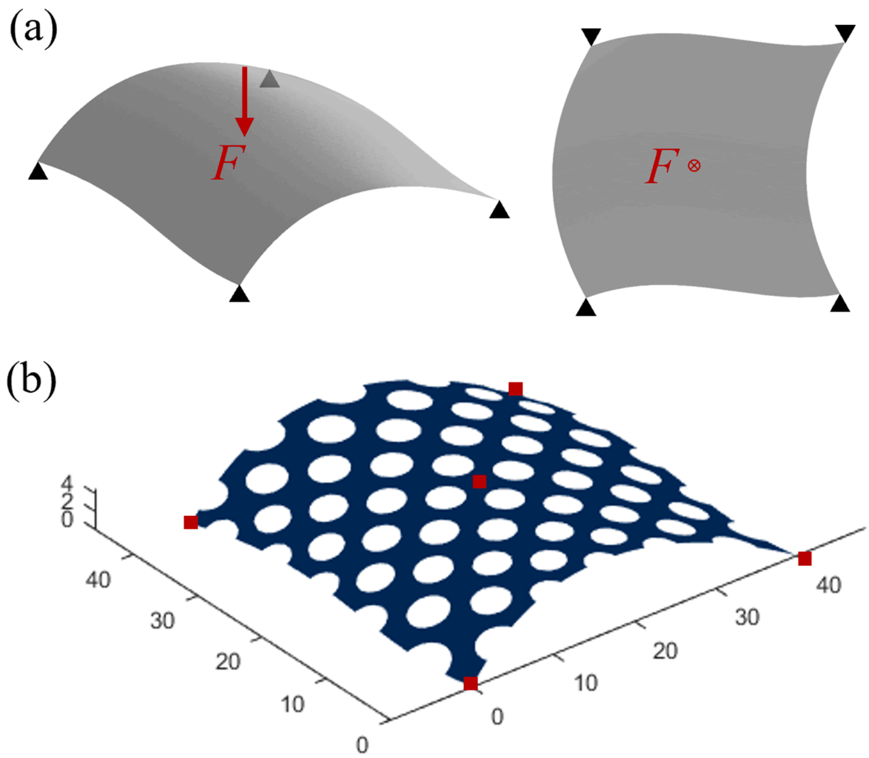

Fig. 13. Constraint conditions and initial design of the curved shell.

constrain the four corner points of the roof and apply multiple vertically downward concentrated loads $F = 1000\text{N}$. The roof is discretized into 59×39 2-order NURBS elements, and the target optimization volume is 0.5. Fig. 16(b) shows the initial design of the roof, which consists of staggered holes. To verify the stability of this optimization method, we apply the loads to the hole regions, as shown by the highlighted constrained areas in the figure.

Similarly, the historical and final optimized results for the Scordelis–Lo Roof are shown in Fig. 17. In the initial phase of optimization, material in unconstrained regions is rapidly removed, while material in loaded regions gradually concentrates. By the 30th iteration, superfluous boundaries have disappeared, and the preliminary configuration emerges. After the 50th iteration, the topological features of the structure gradually stabilize. At the end of the 164th iteration, the optimal result is determined. Finally, the optimized roof in 3D space is obtained through inverse mapping.

As shown in the optimization curves of Fig. 18, the initial design has the highest objective function value. To rapidly reduce the objective function, in the initial optimization phase, material quickly fills the loaded regions. During iterations 1 to 50, the volume ratio and the objective function consistently fluctuate with a negative correlation, and the topological structure changes are relatively drastic during this period. After 80 iterations, the objective function and the volume ratio tend to stabilize, the structure no longer undergoes significant topological changes, and the final result is obtained through continuous fine-tuning of the structure.

4.5.3. Donut shell. Furthermore, we model a donut structure with more complex geometric features and take one-eighth of the donut to simulate a scenario of a heavy object hanging, as shown in Fig. 19(a). The thickness of the donut shell is 1, fixed constraints are applied at both ends, and multiple vertically downward concentrated loads are applied in the middle. The donut shell is divided into 103×73 2-order NURBS elements, and the optimized target volume is 0.5. Fig. 19(b) shows the initial design for the donut shell, which still adopts a staggered arrangement and produces good evolutionary results. The constrained regions are highlighted in the figure.

Fig. 20 shows the historical and final optimized results of the donut shell. In the early stages of optimization, the boundaries of the topological holes expand to satisfy the volume constraint. In the historical results of the 10th and 15th iterations, we can observe that the material in the unconstrained regions on both sides is removed, and the material evolves and merges towards the direction of force transmission. After the 20th iteration, the external boundary is basically stable, and many holes still exist internally. After 80 iterations, all topological features stabilize, and subsequent iterations only make subtle adjustments to the structure. The final result is obtained after 300 iterations, and the optimized donut shell in 3D space is acquired through inverse mapping.

Notably, as the complexity of the design domain increases, the number of iterations rises accordingly, with a corresponding slight impact on the convergence of the algorithm. On the one hand, compared to traditional LSM-based TO, the introduction of conformal mapping may introduce a certain degree of distortion into the velocity field. Shells characterized by more complex geometric features tend to exhibit more pronounced distortion after mapping, consequently requiring additional iterative steps to effectively explore the optimal solution path. On the other hand, mesh refinement increases the number of design variables, which allows for more precise

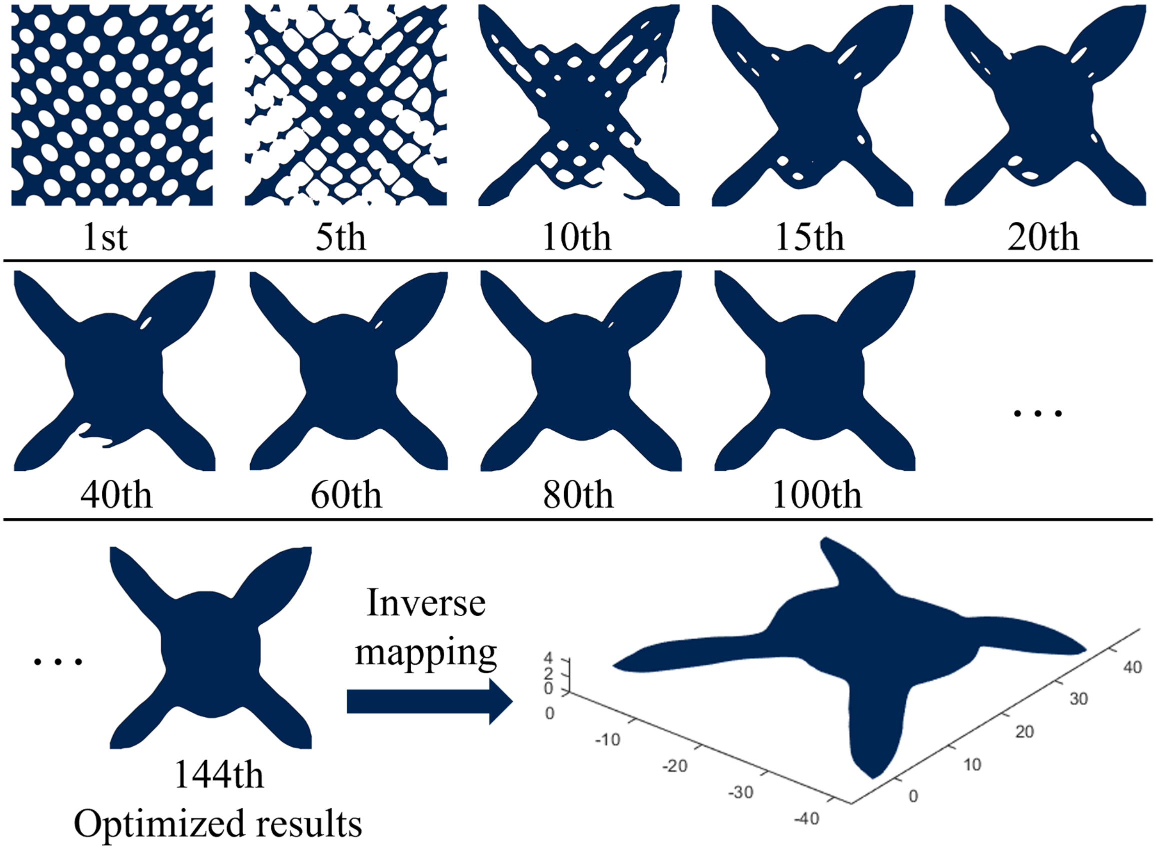

Fig. 14. The historical and final results of the curved shell.

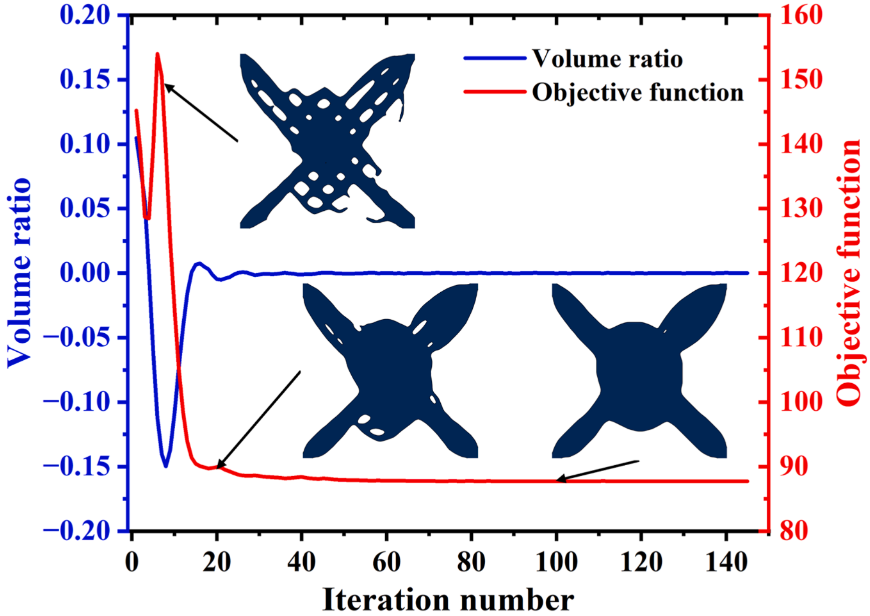

Fig. 15. Optimization curve of the curved shell.

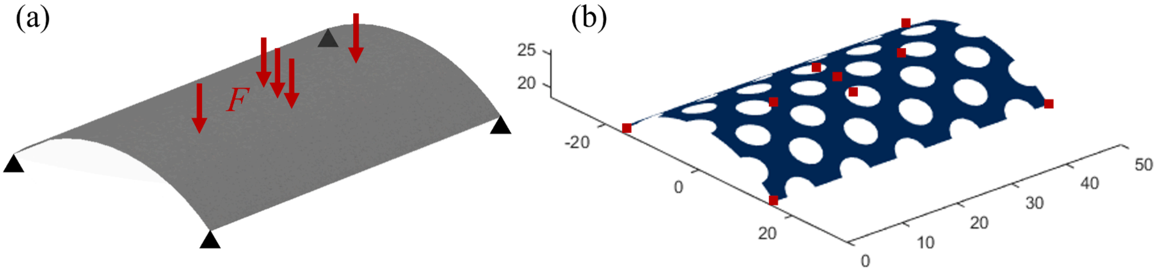

Fig. 16. Constraint conditions and initial design of the Scordelis–Lo Roof.

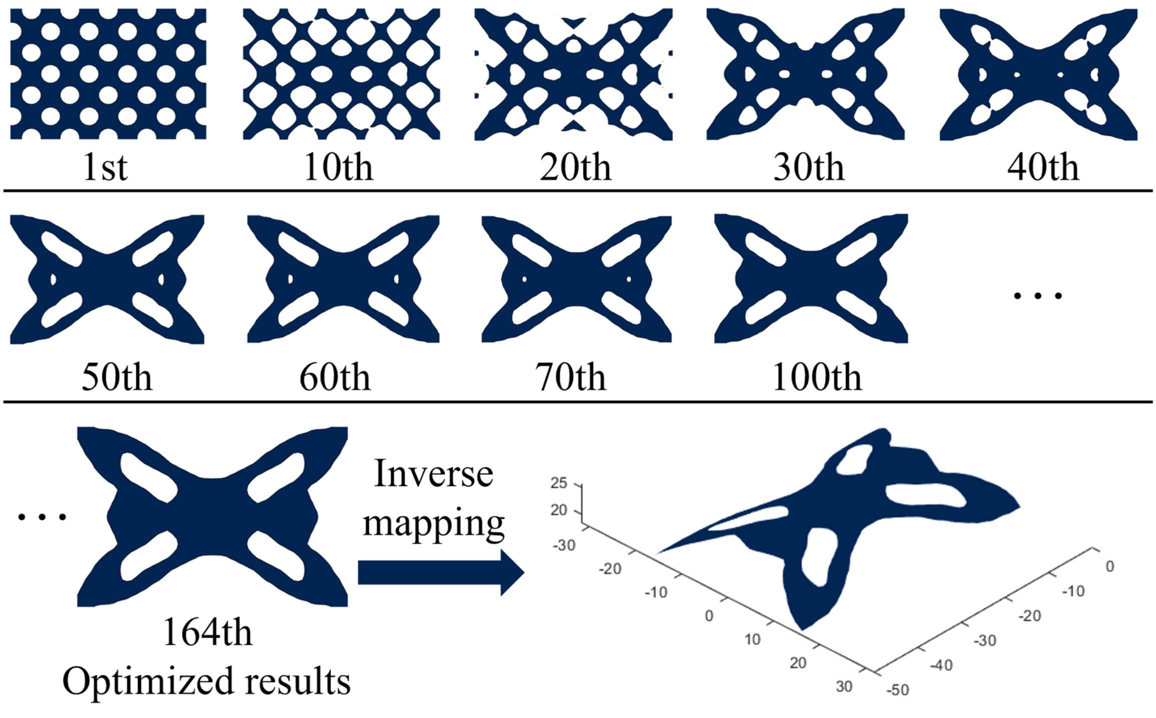

Fig. 17. The historical and final results of the Scordelis–Lo Roof.

solutions but also requires more iterations to converge, as shown in Fig. 12. This challenge is commonly encountered in TO.

Fig. 21 displays the optimization curves for the donut shell. As material aggregates towards the direction of force transmission, the volume decreases, and the objective function also decreases simultaneously; subsequently, both exhibit a negatively correlated fluctuation phenomenon. After 40 iterations of optimization, the volume ratio and the objective function gradually stabilize, and the main topological features of the structure are already stable. After 50 iterations, the changes in the topological features become slower, slightly affecting the optimization efficiency. This is limited by the parameter settings of the optimizer, and the issue can be improved by adjusting these parameters. It is worth noting that, in subsequent iterations, the objective function consistently decreases, demonstrating that the optimization path is stable and steadily converging toward the optimal solution.

5. Conclusions

This paper proposes an ITO method suitable for arbitrarily smooth shells by integrating IGA and conformal mapping-enhanced LSM. To accurately represent the geometric features of the smooth shell, an isogeometric Kirchhoff-Love shell is constructed using NURBS basis function, guaranteeing high-order continuity of the shell elements and ensuring a consistent representation for both geometry and analysis. The introduction of conformal mapping effectively reduces the computational cost of LSM-based TO, enabling 3D smooth shell optimization through 2D design domain solutions while maintaining explicit boundary in 2D results and preserving critical geometric features in 3D optimized shells. The numerical examples validate the accuracy and efficiency of IGA for shell problems. Then, the sensitivity of the proposed ITO method to the initial design is discussed, and the robustness of the conformal mapping is demonstrated based on optimization cases of smooth shells with different geometric features.

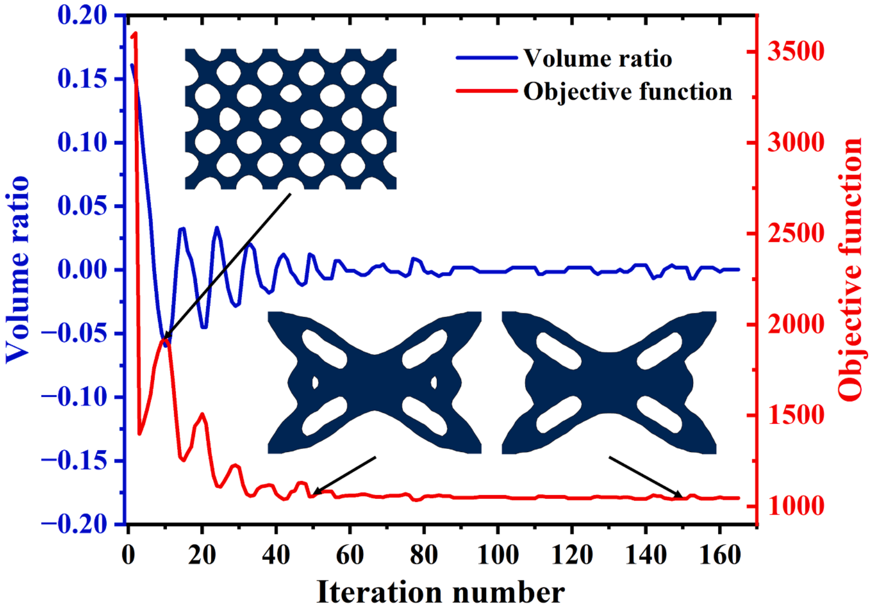

Fig. 18. Optimization curve of the Scordelis–Lo Roof.

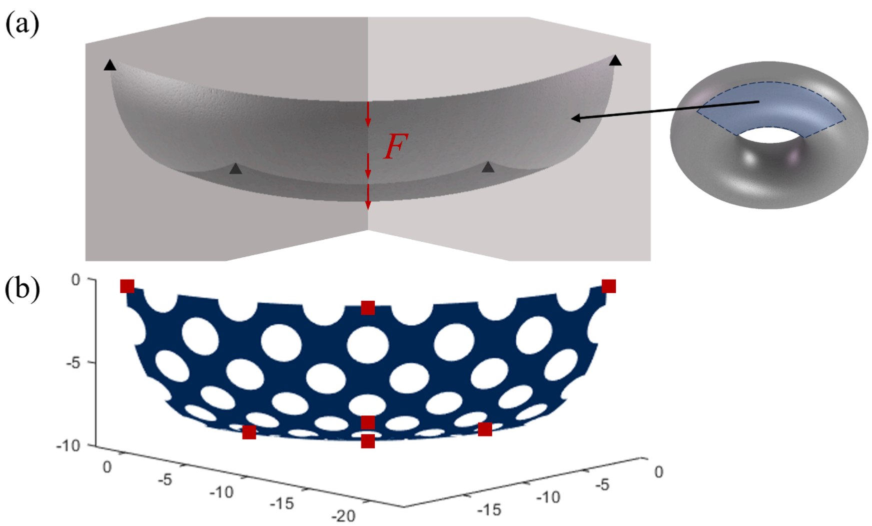

Fig. 19. Constraint conditions and initial design of the donut shell.

The ITO framework proposed in this paper, while ensuring accurate geometric representation, also introduces certain limitations. Firstly, mesh-dependence is not sufficiently suppressed, which can lead to instabilities in the optimization results. Consequently, additional constraint schemes are necessary to mitigate this issue. Secondly, although the conformal mapping-enhanced LSM reduces the computational cost to some extent, the overall optimization efficiency remains relatively low. This indicates a need for further improvements in adaptive parameter tuning strategies.

Future research will focus on extending the methodology to encompass dynamic loading conditions, multi-material coupling systems, multi-resolution and multi-scale optimization frameworks. Adaptive conformal mapping algorithms will be developed to handle non-uniform geometric features. Notably, the ITO-based shell design approach demonstrates significant advantages in CAD reconstruction, establishing foundational prerequisites for practical engineering applications.

CRediT authorship contribution statement

Zhi Xing: Writing – original draft, Software, Formal analysis, Data curation, Conceptualization. **Yingjun Wang:** Writing – review &

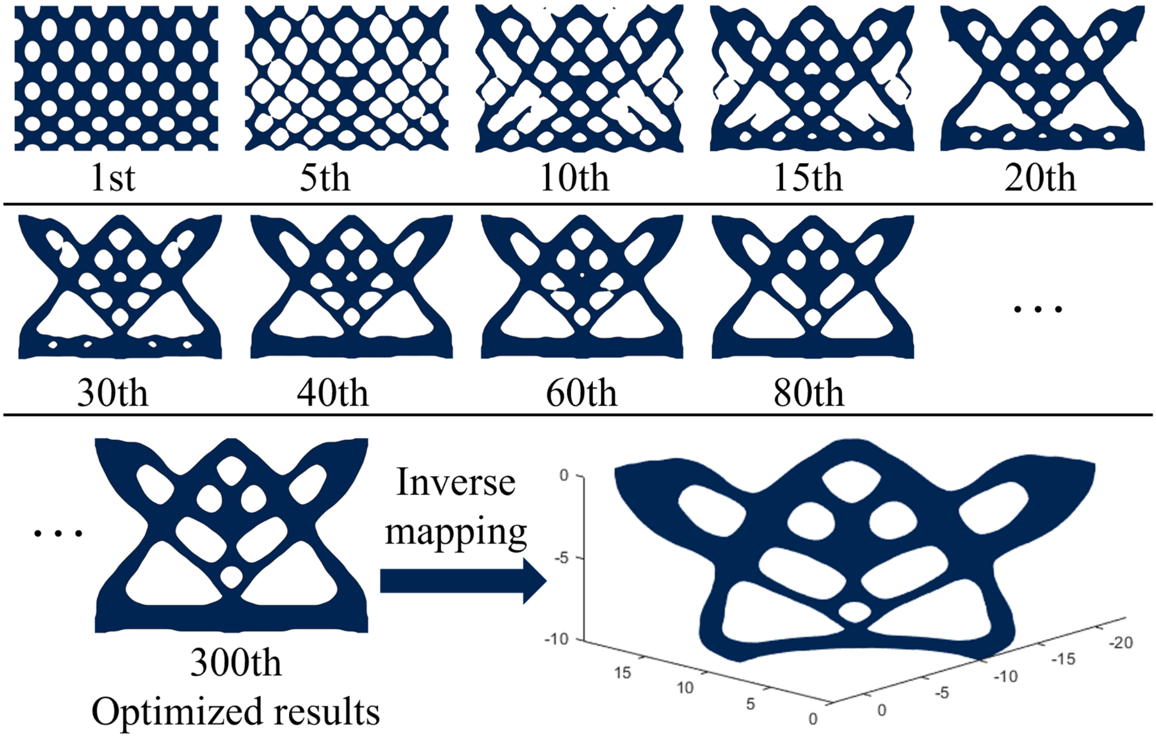

Fig. 20. The historical and final results of the donut shell.

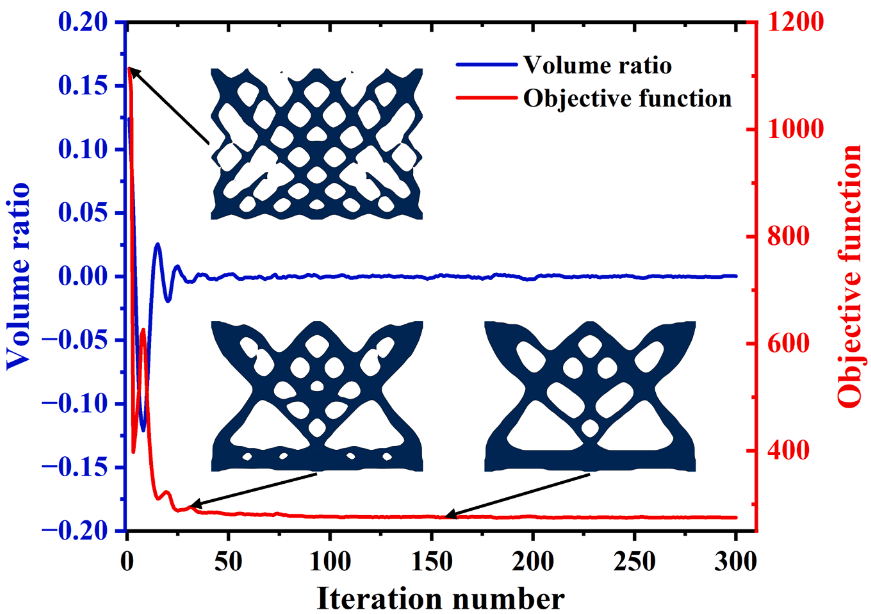

Fig. 21. Optimization curve of the donut shell.

editing, Validation, Supervision, Resources, Funding acquisition.

Declaration of competing interest

The authors declare that they have no known competing financial interests or personal relationships that could have appeared to influence the work reported in this paper.

Acknowledgements

This work has been supported by the Guangdong Basic and Applied Basic Research Foundation (2024A1515011786 and 2025A1515010672).

Supplementary materials

Supplementary material associated with this article can be found, in the online version, at doi:10.1016/j.apm.2025.116504.

Data availability

Data will be made available on request.

References

[1] G.W. Kim, Y.I. Park, K. Park, Topology optimization and additive manufacturing of automotive component by coupling kinetic and structural analyses, Int. J. Automot. Technol. 21 (2020) 1455–1463, https://doi.org/10.1007/s12239-020-0137-1.
[2] A.M. Baghbanan, M. Alaghmandan, M. Golabchi, F. Barazandeh, Architectural form finding and computational design of tall building applying topology optimization against lateral loads, J. Archit. Eng. 29 (2023) 04022038, https://doi.org/10.1061/JAEIED.AEENG-1380.
[3] J. Bai, Y. Zhao, G. Meng, W. Zuo, Bridging topological results and thin-walled frame structures considering manufacturability, J. Mech. Des. 143 (2021) 091706, https://doi.org/10.1115/1.4050300.
[4] D.J. Munk, D.J. Auld, G.P. Steven, G.A. Vio, On the benefits of applying topology optimization to structural design of aircraft components, Struct. Multidiscip. Optim. 60 (2019) 1245–1266, https://doi.org/10.1007/s00158-019-02250-6.
[5] J.H. Zhu, W.H. Zhang, L. Xia, Topology optimization in aircraft and aerospace structures design, Arch. Comput. Method Eng 23 (2016) 595–622, https://doi.org/10.1007/s11831-015-9151-2.
[6] D.J. Benson, Y. Bazilevs, M.C. Hsu, T.J.R. Hughes, Isogeometric shell analysis: the reissner–mindlin shell, Comput. Methods Appl. Mech. Eng. 199 (2010) 276–289, https://doi.org/10.1016/j.cma.2009.05.011.
[7] J. Kiendl, K.U. Bletzinger, J. Linhard, R. Wüchner, Isogeometric shell analysis with Kirchhoff–Love elements, Comput. Methods Appl. Mech. Eng. 198 (2009) 3902–3914, https://doi.org/10.1016/j.cma.2009.08.013.
[8] J.A. Cottrell, T.J.R. Hughes, Y. Bazilevs, Isogeometric analysis: Toward integration of CAD and FEA, 1st ed., Wiley Publishing, 2009.
[9] T.J.R. Hughes, J.A. Cottrell, Y. Bazilevs, Isogeometric analysis: CAD, finite elements, NURBS, exact geometry and mesh refinement, Comput. Methods Appl. Mech. Eng. 194 (2005) 4135–4195, https://doi.org/10.1016/j.cma.2004.10.008.
[10] S. Lipton, J.A. Evans, Y. Bazilevs, T. Elguedj, T.J.R. Hughes, Robustness of isogeometric structural discretizations under severe mesh distortion, Comput. Methods Appl. Mech. Eng. 199 (2010) 357–373, https://doi.org/10.1016/j.cma.2009.01.022.
[11] I. Akkerman, Y. Bazilevs, V.M. Calo, T.J.R. Hughes, S. Hulshoff, The role of continuity in residual-based variational multiscale modeling of turbulence, Comput. Mech. 41 (2008) 371–378, https://doi.org/10.1007/s00466-007-0193-7.
[12] E. Wobbes, Y. Bazilevs, T. Kuraishi, Y. Otoguro, K. Takizawa, T.E. Tezduyar, Complex-geometry IGA mesh generation: application to structural vibrations, Comput. Mech. 74 (2024) 247–261, https://doi.org/10.1007/s00466-023-02432-6.
[13] M. Carraturo, M. Torre, C. Giannelli, A. Reali, An isogeometric approach to coupled thermomechanics in 3D via hierarchical adaptivity, Comput. Math. Appl. 162 (2024) 133–144, https://doi.org/10.1016/j.camwa.2024.02.050.
[14] M. Guerder, A. Duval, T. Elguedj, D. Dam, Volumetric embedded entities for the IsoGeometric analysis of complex structures, Comput. Methods Appl. Mech. Eng. 417 (2023) 116426, https://doi.org/10.1016/j.cma.2023.116426.
[15] L. Piegl, W. Tiller, The NURBS book, Springer, Berlin, Heidelberg, 1997, https://doi.org/10.1007/978-3-642-59223-2.
[16] J. Kiendl, Y. Bazilevs, M.-C. Hsu, R. Wüchner, K.-U. Bletzinger, The bending strip method for isogeometric analysis of kirchhoff–love shell structures comprised of multiple patches, Comput. Methods Appl. Mech. Eng. 199 (2010) 2403–2416, https://doi.org/10.1016/j.cma.2010.03.029.
[17] A. Farahat, H.M. Verhelst, J. Kiendl, M. Kapl, Isogeometric analysis for multi-patch structured Kirchhoff–Love shells, Comput. Methods Appl. Mech. Eng. 411 (2023) 116060, https://doi.org/10.1016/j.cma.2023.116060.
[18] J. Kiendl, M.-C. Hsu, M.C.H. Wu, A. Reali, Isogeometric Kirchhoff–Love shell formulations for general hyperelastic materials, Comput. Methods Appl. Mech. Eng. 291 (2015) 280–303, https://doi.org/10.1016/j.cma.2015.03.010.
[19] T.M. Le, H. Nguyen-Xuan, L. Leonetti, A new paradigm coupling element-wise discrete-strain gaps with patch-wise reduced integration for efficient isogeometric nonlinear kirchhoff–love shell analysis, Comput. Methods Appl. Mech. Eng. 436 (2025) 117667, https://doi.org/10.1016/j.cma.2024.117667.
[20] L. Leonetti, D. Magisano, G. Garcea, Large rotation isogeometric shell model for alternating stiff/soft curved laminates including warping and interlayer thickness change, Comput. Methods Appl. Mech. Eng. 424 (2024) 116908, https://doi.org/10.1016/j.cma.2024.116908.
[21] M.D. Alaydin, Y. Bazilevs, Multilayer shells interacting through friction, J. Appl. Mech. 90 (2023), https://doi.org/10.1115/1.4062139.
[22] H. Mohammadi, M. Shojaee, Y. Kiani, A simplified isogeometric approach for vibrational analysis of nanocomposite panels with a free-form curve, Thin Walled Struct. 183 (2023) 110426, https://doi.org/10.1016/j.tws.2022.110426.
[23] M.P Bendsøe, O. Sigmund, Topology Optimization, Springer, Berlin, Heidelberg, 2004, https://doi.org/10.1007/978-3-662-05086-6.
[24] G. Allaire, R.V. Kohn, Topology optimization and optimal shape design using homogenization, in: M.P. Bendsøe, C.A.M. Soares (Eds.), Topology Design of Structures, Springer Netherlands, Dordrecht, 1993, pp. 207–218, https://doi.org/10.1007/978-94-011-1804-0_14.
[25] O. Sigmund, Design of Material Structures Using Topology Optimization, Doctor, Technical University of Denmark, 1994.
[26] B. Hassani, S.M. Tavakkoli, N.Z. Moghadam, Application of isogeometric analysis in structural shape optimization, Scientia Iranica 18 (2011) 846–852, https://doi.org/10.1016/j.scient.2011.07.014.
[27] J. López, C. Anitescu, T. Rabczuk, Isogeometric structural shape optimization using automatic sensitivity analysis, Appl. Math Model. 89 (2021) 1004–1024, https://doi.org/10.1016/j.apm.2020.07.027.
[28] W.A. Wall, M.A. Frenzel, C. Cyron, Isogeometric structural shape optimization, Comput. Methods Appl. Mech. Eng. 197 (2008) 2976–2988, https://doi.org/10.1016/j.cma.2008.01.025.
[29] Y. Wang, Z. Wang, Z. Xia, L. Poh, Structural design optimization using isogeometric analysis: A comprehensive review, CMES 117 (2018) 455–507, https://doi.org/10.31614/cmes.2018.04603.
[30] B. Hassani, M. Khanzadi, S.M. Tavakkoli, An isogeometrical approach to structural topology optimization by optimality criteria, Struct. Multidisc. Optim. 45 (2012) 223–233, https://doi.org/10.1007/s00158-011-0680-5.
[31] Q.X. Lieu, J. Lee, A multi-resolution approach for multi-material topology optimization based on isogeometric analysis, Comput. Methods Appl. Mech. Eng. 323 (2017) 272–302, https://doi.org/10.1016/j.cma.2017.05.009.

[32] Q.X. Lieu, J. Lee, Multiresolution topology optimization using isogeometric analysis, Int. J. Numer. Methods Eng. 112 (2017) 2025–2047, https://doi.org/10.1002/nme.5593.
[33] Y. Wang, H. Xu, D. Pasini, Multiscale isogeometric topology optimization for lattice materials, Comput. Methods Appl. Mech. Eng. 316 (2017) 568–585, https://doi.org/10.1016/j.cma.2016.08.015.
[34] J. Gao, Z. Luo, M. Xiao, L. Gao, P. Li, A NURBS-based multi-material interpolation (N-MMI) for isogeometric topology optimization of structures, Appl. Math. Model. 81 (2020) 818–843, https://doi.org/10.1016/j.apm.2020.01.006.
[35] Y. Wang, Z. Liao, M. Ye, Y. Zhang, W. Li, Z. Xia, An efficient isogeometric topology optimization using multilevel mesh, MGCG and local-update strategy, Adv. Eng. Softw. 139 (2020) 102733, https://doi.org/10.1016/j.advengsoft.2019.102733.
[36] Y. Wang, M. Xiao, Z. Xia, P. Li, L. Gao, From computer-aided design (CAD) toward Human-aided design (HAD): an isogeometric topology optimization approach, Engineering 22 (2023) 94–105, https://doi.org/10.1016/j.eng.2022.07.013.
[37] J. Yang, H. Su, X. Li, Y. Wang, Fail-safe topology optimization for multiscale structures, Comput. Struct. 284 (2023) 107069, https://doi.org/10.1016/j.compstruc.2023.107069.
[38] J. Gao, L. Gao, Z. Luo, P. Li, Isogeometric topology optimization for continuum structures using density distribution function, Int. J. Numer. Methods Eng. 119 (2019) 991–1017, https://doi.org/10.1002/nme.6081.
[39] M.Y. Wang, X. Wang, D. Guo, A level set method for structural topology optimization, Comput. Methods Appl. Mech. Eng. 192 (2003) 227–246, https://doi.org/10.1016/S0045-7825(02)00559-5.
[40] S. Shojaee, M. Mohamadian, N. Valizadeh, Composition of isogeometric analysis with level set method for structural topology optimization, (n.d.).
[41] Y. Wang, D.J. Benson, Isogeometric analysis for parameterized LSM-based structural topology optimization, Comput. Mech. 57 (2016) 19–35, https://doi.org/10.1007/s00466-015-1219-1.
[42] Y. Wang, D.J. Benson, Geometrically constrained isogeometric parameterized level-set based topology optimization via trimmed elements, Front. Mech. Eng. 11 (2016) 328–343, https://doi.org/10.1007/s11465-016-0403-0.
[43] F.H. Scherer, M. Zarroug, H. Naceur, A. Constantinescu, Stress-based topological shape optimization for thick shells using the level set method and trimmed non-conforming multi-patch isogeometric analysis, Struct. Multidisc. Optim. 67 (2024) 177, https://doi.org/10.1007/s00158-024-03892-x.
[44] F.H. Scherer, M. Zarroug, H. Naceur, A. Constantinescu, Topology optimization of curved thick shells using level set method and non-conforming multi-patch isogeometric analysis, Comput. Methods Appl. Mech. Eng. 430 (2024) 117205, https://doi.org/10.1016/j.cma.2024.117205.
[45] Q. Ye, Y. Guo, S. Chen, N. Lei, X.D. Gu, Topology optimization of conformal structures on manifolds using extended level set methods (X-LSM) and conformal geometry theory, Comput. Methods Appl. Mech. Eng. 344 (2019) 164–185, https://doi.org/10.1016/j.cma.2018.08.045.
[46] X. Gu, Y. Wang, T.F. Chan, P.M. Thompson, S.-T. Yau, Genus zero surface conformal mapping and its application to brain surface mapping, IEEE Trans. Med. Imaging 23 (2004) 949–958, https://doi.org/10.1109/TMI.2004.831226.
[47] X.D. Gu, F. Luo, S.T. Yau, Recent advances in computational conformal geometry, Commun. Inf. Syst. 9 (2009) 163–196, 201308301624.
[48] X.D. Gu, S.T. Yau, Computational Conformal Geometry, International Press of Boston, 2008. https://book.douban.com/subject/4584701/. accessed July 27, 2022.
[49] X.D. Gu, W. Zeng, F. Luo, S.T. Yau, Numerical computation of surface conformal mappings, Comput. Methods Funct. Theory 11 (2012) 747–787, https://doi.org/10.1007/BF03321885.
[50] J. Tian, M. Li, Z. Han, Y. Chen, X.D. Gu, Q.J. Ge, S. Chen, Conformal topology optimization of multi-material ferromagnetic soft active structures using an extended level set method, Comput. Methods Appl. Mech. Eng. 389 (2022) 114394, https://doi.org/10.1016/j.cma.2021.114394.
[51] X. Xu, X.D. Gu, S. Chen, Shape and topology optimization of conformal thermal control structures on free-form surfaces: A dimension reduction level set method (DR-LSM), Comput. Methods Appl. Mech. Eng. 398 (2022) 115183, https://doi.org/10.1016/j.cma.2022.115183.
[52] J. Ding, Z. Zeng, Z. Xing, W. Nong, F. Wu, Discrete level set method enhanced by conformal mapping: an efficient approach for topology optimization of piezoelectric energy harvesters, Struct. Multidisc. Optim. 67 (2024) 173, https://doi.org/10.1007/s00158-024-03893-w.
[53] P.M. Naghdi, The theory of shells and plates, in: C. Truesdell (Ed.), Linear Theories of Elasticity and Thermoelasticity: Linear and Nonlinear Theories of Rods, Plates, and Shells, Springer, Berlin, Heidelberg, 1973, pp. 425–640, https://doi.org/10.1007/978-3-662-39776-3_5.
[54] S.J. Osher, R.P. Fedkiw, Level Set Methods and Dynamic Implicit Surfaces, Springer, 2002. https://book.douban.com/subject/2858262/. accessed August 9, 2023.
[55] R. Sawhney, K. Crane, Boundary first flattening, ACM Trans. Graph. 37 (2018) 1–14, https://doi.org/10.1145/3132705.
[56] T.W. Meng, G.P.T. Choi, L.M. Lui, TEMPO: feature-endowed Teichmüller Extremal mappings of point clouds, SIAM J. Imaging Sci. 9 (2016) 1922–1962, https://doi.org/10.1137/15M1049117.
[57] P.T. Choi, L.M. Lui, Fast disk conformal parameterization of simply-connected open surfaces, J. Sci. Comput. 65 (2015) 1065–1090, https://doi.org/10.1007/s10915-015-9998-2.
[58] Y. Wang, Z. Kang, MATLAB implementations of velocity field level set method for topology optimization: an 80-line code for 2D and a 100-line code for 3D problems, Struct. Multidisc. Optim. 64 (2021) 4325–4342, https://doi.org/10.1007/s00158-021-02958-4.
[59] Y. Wang, Z. Kang, A velocity field level set method for shape and topology optimization, Int. J. Numer. Methods Eng. 115 (2018) 1315–1336, https://doi.org/10.1002/nme.5845.
[60] K. Svanberg, The method of moving asymptotes—a new method for structural optimization, (n.d.). https://doi.org/10.1002/nme.1620240207.
[61] R.H. Macneal, R.L. Harder, A proposed standard set of problems to test finite element accuracy, Finite, Elem. Anal. Des. 1 (1985) 3–20, https://doi.org/10.1016/0168-874X(85)90003-4.
[62] T. Ho-Nguyen-Tan, H.-G. Kim, An efficient method for shape and topology optimization of shell structures, Struct. Multidisc. Optim. 65 (2022) 119, https://doi.org/10.1007/s00158-022-03213-0.
[63] X. Zhang, M. Xiao, L. Gao, J. Gao, A T-splines-oriented isogeometric topology optimization for plate and shell structures with arbitrary geometries using bézier extraction, Comput. Methods Appl. Mech. Eng. 425 (2024) 116929, https://doi.org/10.1016/j.cma.2024.116929.
[64] S. Cai, H. Zhang, W. Zhang, An integrated design approach for simultaneous shape and topology optimization of shell structures, Comput. Methods Appl. Mech. Eng. 415 (2023) 116218, https://doi.org/10.1016/j.cma.2023.116218.
[65] O. Sigmund, J. Petersson, Numerical instabilities in topology optimization: a survey on procedures dealing with checkerboards, mesh-dependencies and local minima, Struct. Optim. 16 (1998) 68–75, https://doi.org/10.1007/BF01214002.